



CHALMERS
UNIVERSITY OF TECHNOLOGY

Numerical simulations of the tip leakage vortex in a waterjet pump using a Reynolds averaged approach

Master's thesis in Mechanics and Maritime Sciences

LUCÍA LEÓN CALDERÓN

REPORT NO. 2019:44

Numerical simulations of the tip leakage vortex in a waterjet pump using a Reynolds averaged approach

Master's Thesis in Mechanics and Maritime Sciences

LUCÍA LEÓN CALDERÓN

Department of Mechanics and Maritime Sciences
CHALMERS UNIVERSITY OF TECHNOLOGY
Gothenburg, Sweden 2019

Numerical simulations of the tip leakage vortex in a waterjet pump using a Reynolds averaged approach
LUCÍA LEÓN CALDERÓN

© LUCÍA LEÓN CALDERÓN, 2019.

Technical report no 2019:44
Department of Mechanics and Maritime Sciences
Chalmers University of Technology
SE-412 96 Göteborg Sweden
Telephone + 46 (0)31-772 1000

Numerical simulations of the tip leakage vortex in a waterjet pump using a Reynolds averaged approach

LUCÍA LEÓN CALDERÓN

Department of Applied Mechanics and Maritime Sciences
Chalmers University of Technology

Abstract

Waterjet pumps are widely used among maritime transport vehicles, such as high-speed vessels. Many experiments have been performed to analyze the complex flow patterns present in these axial pumps, such as the tip leakage vortex (TLV) [1, 2]. Experiments are time and resource consuming, which is pushing the use of computational methods in order to provide accurate and faster results.

The aim of this project is to provide a good prediction of the TLV structures using Reynolds Averaged Navier Stokes models (RANS) within steady and unsteady conditions by validating with experimental data provided in Li et. al [1]. The studies include Multiple Reference Frame (MRF) approach for steady mode and Sliding Mesh (SM) for unsteady mode. The $k - \omega SST$ turbulence model is used as a baseline for both configurations although two additional variations will be tested: $k - \omega SST$ with Curvature Correction (CC) for the steady mode and the $k - \omega SST$ Scale Adaptive Simulation (SAS) for unsteady mode.

Concerning mesh resolution, 40 cells in the radial direction covering the tip gap are sufficient to obtain good agreement with experiment. Additionally, the optimum divergence scheme is the limitedLinear scheme as it provides qualitative good agreement.

Using the resulting mesh and the chosen scheme, unsteady simulations showed to improve the agreement with experimental data compared to steady simulations. Also, the CC and SAS turbulence models proved to be less adequate for TLV prediction in comparison with the $k - \omega SST$ model.

Additionally, some parametrical studies are performed in steady mode including the Boundary Layer (BL) thickness analysis and blade tip shape effect on the TLV. It is concluded that there is no qualitative difference for different inlet BL thickness. On the other hand, blade shape highly influences the TLV. Rounded blade tip edges increase the tip clearance flow leading to a stronger TLV with a core further into the core flow passage. This is related to a reduction in the recirculation flow in the tip clearance.

Keywords: Waterjet Pump, RANS, Tip Leakage Vortex, MRF, Sliding Mesh, CFD.

TABLE OF CONTENTS

Table of contents	III
Acknowledgements.....	I
Physical quantities.....	II
List of abbreviations	III
1. Introduction.....	1
1.1. Background.....	1
1.2. Introduction to waterjet pumps	1
1.2.1. The AxWJ-2 waterjet pump	2
1.3. Aim.....	3
1.4. Delimitations	4
1.5. Specification of issue under investigation	4
2. Computational methods	5
2.1. Reynolds Averaged Navier Stokes models (RANS)	5
2.2. Rotation approaches	6
2.2.1. Multiple Reference Frame (MRF)	6
2.2.2. Sliding mesh	6
3. Methodology	7
3.1. Simulation workflow.....	7
3.2. Geometry.....	7
3.3. Mesh.....	8
3.4. Set-up	10
3.4.1. Steady RANS.....	10
3.4.2. Unsteady RANS	12
3.4.3. Summary	13
4. Steady RANS simulations	15
4.1. Validation of results.....	15
4.1.1. Performance prediction	15
4.1.2. TLV structures	15
4.2. Sensitivity analysis	18
4.2.1. Boundary layer thickness.....	18
4.2.2. Inlet velocity profile	24
4.2.3. Turbulence model	27
4.2.4. Mesh refinement	29
4.3. Wall functions.....	32
4.4. Rotor-stator interface.....	33
4.5. Blade geometry	36

4.5.1.	Performance	37
4.5.2.	SPIV planes.....	38
4.6.	Grid convergence study	40
5.	Unsteady RANS simulations.....	41
5.1.	Validation of results.....	41
5.1.1.	Performance prediction	41
5.1.2.	TLV structures	41
5.2.	Turbulence model comparison.....	44
5.2.1.	Performance prediction	44
5.2.2.	TLV structures	45
6.	Conclusions.....	47
	References	49
	Appendix I: Reynolds stresses derivation.....	51

ACKNOWLEDGEMENTS

First, I would like to thank my home university, Universidad Politécnica de Madrid, and Chalmers University of Technology for providing me with the chance of finishing here my studies and developing this project.

It has been a wonderful challenge and has provided me with much more knowledge and experience than I ever expected. But it wouldn't have been possible without the help of my supervisors.

Thank you, Mohammad, for teaching me everything you knew and sharing your 'tips and tricks' with me, for your patience and your hard work. And also to you, Håkan, for pushing me to make things always as perfect as possible.

To my friends, the ones I left back home and the ones I have met here, who have helped me disconnect from work from time to time.

However, I wouldn't have come so far if it wasn't for my family. Everything I have achieved during these years is also yours, thank you for your unconditional support.

Muchas gracias a todos.

PHYSICAL QUANTITIES

φ – Flow coefficient
 ψ – Head coefficient
 η – Efficiency
 N – Rotational speed (rps)
 ρ – Density (kg/m^3)
 p – Pressure (Pa)
 g – Gravity (m/s^2)
 D_3 – Diameter of the impeller (m)
 I – Turbulent intensity (%)
 k – Turbulent kinetic energy (m^2/s^2)
 ω – Specific dissipation rate (s^{-1})
 ε – Dissipation rate (m^2/s^3)
 y^+ – Wall non-dimensional distance
 Φ – Flow rate (m^3/s)
 Q_{BEP} – Flow rate at the best efficiency point (m^3/s)
 D_{shaft} – Shaft diameter (m)
 u_{inlet} – Inlet velocity (m/s)
 U – Mean velocity in absolute frame of reference (m/s)
 u' – Fluctuating velocity in absolute frame of reference (m/s)
 ν_t – Turbulent kinematic viscosity (m^2/s)
 ν – Kinematic viscosity (m^2/s)
 u_θ – Tangential velocity in absolute frame of reference (m/s)
 u_R – Velocity in the rotating frame of reference (m/s)
 u_I – Velocity in the inertial frame of reference (m/s)
 U_T – Tangential velocity at blade tip (m/s)
 ω_θ – Tangential vorticity in absolute frame of reference (s^{-1})
 h – Tip clearance (m)
 R – Impeller radius (m)
 z – Axial coordinate (m)
 r – Radial coordinate (m)
 U_z – Axial velocity in cylindrical coordinates and absolute frame of reference (m/s)
 Q – Q-criterion (s^{-2})
 r_{21} – Grid refinement ratio between mesh 1 and 2
 r_{32} – Grid refinement ratio between mesh 2 and 3
 P – Order of convergence

LIST OF ABBREVIATIONS

TLV – Tip Leakage Vortex
CFD – Computational Fluid Dynamics
PS – Pressure Side
SS – Suction Side
BEP – Best Efficiency Point
JHU – Johns Hopkins University
RANS – Reynolds Averaged Navier Stokes
MRF – Multiple Reference Frame
LES – Large Eddy Simulation
DNS – Direct Numerical Simulation
SST – Shear Stress Transport
SM – Sliding Mesh
CAD – Computer Aided Design
SIMPLE – Semi-Implicit Method for Pressure Linked Equations
PCG – Preconditioned Conjugate Gradient
GAMG – Geometric Agglomerated algebraic Multigrid
PBiCCCG – Preconditioned Bi-Conjugate Gradient solver
SPIV – Stereoscopic Particle Image Velocimetry
BL – Boundary Layer
LE – Leading Edge
CC – Curvature Correction
TKE – Turbulent Kinetic Energy
GCI – Grid Convergence Index
TE – Trailing Edge
URANS – Unsteady Reynolds Averaged Navier-Stokes
SAS – Scale Adaptive Simulation

1. INTRODUCTION

1.1. Background

Maritime transit of passengers in Europe has suffered a recession in the last decade. Actions like the abolition of the duty-free regime and a hard competition against low-cost airlines, among others, have produced this drop in the ferry industry. Due to this, operators have to face a reduction of the ticket prices to be competitive against land and air transportation [3].

In order to reduce ticket prices, operators are seeking for more powerful propulsion systems with a wide working range to reduce costs as well as travelling time. Following this trend, manufacturers like Rolls Royce are more concerned about providing high-speed propulsion systems together with a wider stable range of working conditions [4, 5].

The major problem associated with the reliability of waterjet pumps is cavitation. In the last years, research has been focused in trying to understand and predict Tip Leakage Vortex (TLV) cavitation, as it can cause severe damage to the pump [6]. TLV cavitation is related to the formation of the TLV, a vortex formed in the gap between the tip of a rotating impeller blade and the shroud casing. The gap between blade and shroud is unavoidable as this limit is defined by manufacturers and mechanical requirements. Then, the only available option to reduce this phenomenon is by understanding how tip leakage vortex affects the main flow and how it can lead to TLV cavitation [6].

Research on waterjet pumps has been done by experiments, method which can be expensive and time consuming. As an alternative, computational methods such as Computational Fluid Dynamics (CFD), have arisen to gain time and reduce costs [7]. As it is still a developing technology, the accuracy of the models is being validated every day with new test cases such as those published by Bulten [8].

Due to the high complexity of simulating TLV cavitation using CFD, an adequate simulation procedure must be defined to assure accurate TLV prediction. That procedure can then be applied to future cavitation studies. The results from this thesis aim to provide that procedure.

1.2. Introduction to waterjet pumps

Waterjet pumps are used nowadays, not only for high-speed vessels, but also for military vessels and ferries, like the Stena High-speed Sea Service. This propulsion system creates a jet of water that pushes the ship forward. The pump can be powered by diesel engines or gas turbines [9].

A waterjet pump set for its commercial application is formed of the following components: inlet, pump, nozzle and steering device. The pump delivers the head to produce the jet of water that flows through the nozzle. The inlet is a duct that collects water from beneath the hull and takes it into the pump inlet. The most common configuration is a flush mounted duct, used for fast ferries. The steering device deflects the jet of water in order to manoeuvre [8].

Performance in a pump can be described using the following dimensionless parameters:

- Flow coefficient φ which is the dimensionless volumetric flow rate, expressed as:

$$\varphi = \frac{\Phi}{ND_3^2}$$

where Φ is the volumetric flow rate (m^3/s), N is the rotational speed (*rps*) and D_3 is the diameter of the impeller (*m*) [10].

1. INTRODUCTION

- Head rise coefficient ψ that is the dimensionless energy transfer of the pump, defined as:

$$\psi = \frac{p_{T,2} - p_{T,1}}{\rho N^2 D_3^2}$$

where $p_{T,2}$ is the total pressure at the exit of the pump and $p_{T,1}$ at the inlet (Pa) and ρ is the density (kg/m^3) [10].

Because of design requirements, these pumps have a clearance between the tip of the blade and the shroud. Due to the pressure difference between the Pressure Side (PS) and Suction Side (SS) of the blade, flow leaks through that clearance (Figure 1). When the tip leakage flow encounters the incoming flow, generated a swirling pattern known as TLV. This vortex can affect the efficiency of the pump and even cause a blockage of the flow [11].

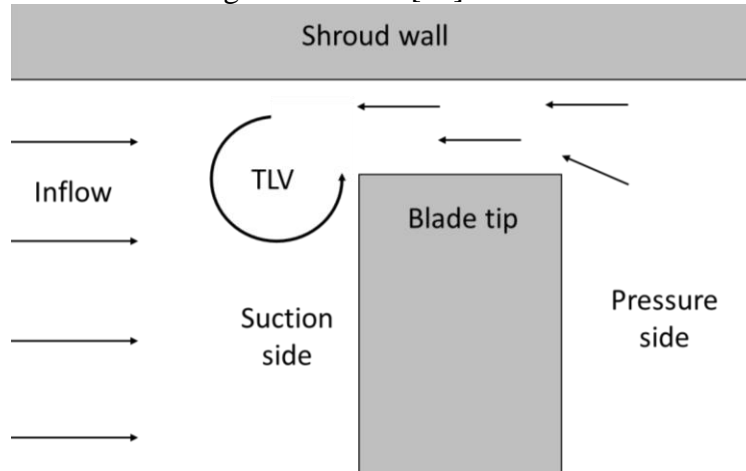


Figure 1. Graphical explanation of tip leakage and TLV.

Furthermore, cavitation is a common problem in these devices producing erosion, noise, vibration and consequently a reduction in efficiency. It is a very complex phenomenon, but it can be divided in three categories: sheet cavitation, back-flow vortex cavitation and TLV cavitation [6]. The TLV cavitation is originated when bubbles created in the tip clearance, get to the SS of the blade entering the passage [2]. These bubbles appear as pressure in the tip clearance is reduced below the saturation pressure. Afterwards, these bubbles incorporate to the TLV and propagate downstream in the passage until a bubbly cloud is formed. Further analysis of the TLV structure will help to develop more cavitation control methods [6].

1.2.1. The AxWJ-2 waterjet pump

The model AxWJ-2 has been involved in many research before, regarding cavitating and non-cavitating TLV analysis, like Tan et al. [10] and Lindau et al. [11] among others. Results in this thesis are validated with the Stereoscopic Particle Image Velocimetry (SPIV) measurements presented in Li et. al [1]. Performance was studied for the AxWJ-2 model using the test rig shown in Figure 2, being reported a flow coefficient (φ) of 0.76 and a head coefficient (ψ) of 2.46 at the Best Efficiency Point (BEP) [2]. The geometrical information and operating parameters of the pump can be seen in Table 1 [2, 10].

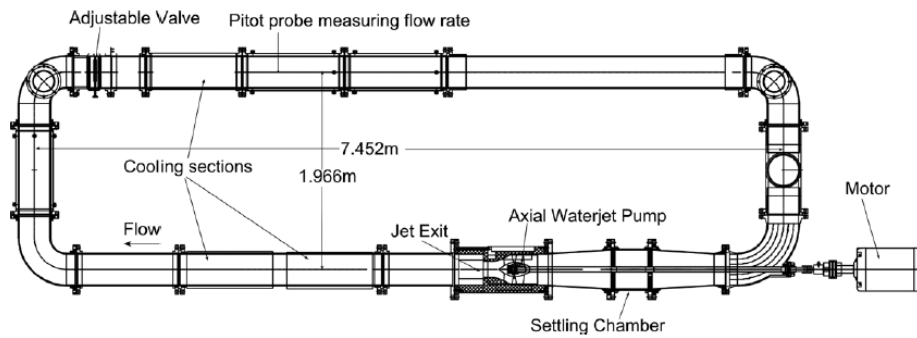


Figure 2. Test rig for the AxWJ-2 waterjet pump in JHU [10].

Inlet section casing diameter D_1	305.2 mm
Outflow section diameter $D_2 = 0.699D_1$	213.4 mm
Pipe inner diameter downstream of the pump D_3	304.8 mm
Diameter of the shaft d	50.8 mm
Rotor diameter D_R	303.8 mm
Number of rotor blades n_R	6
Number of stator blades n_S	8
Tip profile chord length c	274.3 mm
Tip profile axial chord length c_A	127.4 mm
Tip profile stagger angle $\gamma = \arcsin(c_A c^{-1})$	27.7°
Tip profiles pitch $\zeta = \pi D_R n_R^{-1}$	159.1 mm
Tip profile solidity $c \zeta^{-1}$	1.72
Tip clearance h	0.9 mm
Angular speed of the rotor Ω	94.2 rad s ⁻¹ (900 RPM)
Tip speed $U_T = \Omega D_R / 2$	14.32 m s ⁻¹
Tip profile Reynolds number $Re_c = U_T c \nu^{-1}$	3.6 · 10 ⁶

Table 1. Geometric information and operating parameters about the AxWJ-2 waterjet pump [1].

1.3. Aim

The main objective of this project is to provide accurate results of the TLV of the AxWJ-2 pump in order to define an adequate simulation procedure for future cavitation studies. This computational set-up should provide accurate results while reducing the computational costs associated.

In order to obtain this, the following steps should be done:

- Simulate the flow fields of the pump using a steady-state method, with wall functions and RANS models. MRF rotation approach is used. The most adequate set-up will be chosen after performing some parametrical studies and used for unsteady simulations.
- Perform an unsteady simulation using RANS models. Sliding mesh coupling will be used.

1. INTRODUCTION

All simulations will be performed using the open source software OpenFOAM v1706.

1.4. Delimitations

The project concerns numerical simulations, only having experimental data from JHU for validating the results. Therefore, only the experimentally tested model, the AxWJ-2 waterjet, can be studied in the project.

As no information regarding the turbulence intensity at the inlet is provided by Li et al. [1], a value of 5% is assumed. This choice is based on the properties of the settling chamber and two honeycombs that are located before the pump.

Only one operating condition is analysed. Consequently, other possible working conditions are left out of the scope of this project. According to Tan et al. [2], the flow properties are quite similar for other operating conditions.

The geometry available for the project corresponds to the aluminium model which has no rounded edges at the tip of the blade, whereas in the experimental model in Li et. al [1] the geometry has rounded edges. The value of the radius is not reported, so different guesses will be proposed in section 4.5 of the project to analyse the effect of the shape.

Also, the only information about the inlet velocity profile provided from the experiment is at a measurement plane upstream of the rotor where there is a contraction of the inlet channel. This hampers the reproduction of the experimental conditions in the simulation as explained in section 4.2.2.

1.5. Specification of issue under investigation

- Are steady RANS models suitable for predicting the pump performance?
- Is MRF approach adequate for predicting TLV structures?
- Do the results from steady RANS simulations agree with the provided experimental data?
- Is the TLV structure affected by different inlet boundary layer thickness?
- Does the TLV change for different edge shapes on the blade tip?
- Is the prediction of overall performance mesh independent?
- Do unsteady RANS models predict more accurately than steady simulations the development of TLV?

2. COMPUTATIONAL METHODS

Computational Fluid Dynamics (CFD) simulations have been used in the past decades to get a more comprehensive access to flow field. RANS turbulence models have been mainly applied to predict the overall performance of pumps and have showed adequate accuracy [12]. In the following section, the focus will be on RANS models as well as the different rotation approaches used in this project.

2.1. Reynolds Averaged Navier Stokes models (RANS)

When using RANS turbulence models, the Navier-Stokes equations are time-averaged, that is, solving only for the mean flow properties. Turbulence is accounted for in the Reynolds-averaged momentum equations in the form of Reynolds stresses (last term on the right-hand side on Equations 1-3) which result from the averaging procedure. These Reynolds stresses are modelled by RANS turbulence models [13]. The Reynolds-averaged momentum equations for incompressible flows are provided below:

$$\frac{\partial U}{\partial t} + \nabla \cdot (U\mathbf{U}) = -\frac{\partial p}{\rho \partial x} + \nu \nabla \cdot (\nabla U) - \nabla \cdot (\overline{u'\mathbf{u}'})$$

Equation 1. Reynolds-averaged momentum equation for x components [13].

$$\frac{\partial V}{\partial t} + \nabla \cdot (V\mathbf{U}) = -\frac{\partial p}{\rho \partial y} + \nu \nabla \cdot (\nabla V) - \nabla \cdot (\overline{v'\mathbf{u}'})$$

Equation 2. Reynolds-averaged momentum equation for y components [13].

$$\frac{\partial W}{\partial t} + \nabla \cdot (W\mathbf{U}) = -\frac{\partial p}{\rho \partial z} + \nu \nabla \cdot (\nabla W) - \nabla \cdot (\overline{w'\mathbf{u}'})$$

Equation 3. Reynolds-averaged momentum equation for z components [13].

where $\mathbf{U}=(U, V, W)$ is the mean velocity vector, $\mathbf{u}' = (u', v', w')$ is the fluctuating velocity vector, ρ is the density, p is the pressure field and ν is the kinematic viscosity of the fluid.

As all the turbulence is modelled, there is no need to have very fine mesh in the tangential direction close to the wall, therefore requiring much less computational resources than LES or DNS [13]. The wall-normal resolution of the grid can also be reduced drastically when wall functions are used in combination with RANS models.

This type of simulations is mainly used for steady-state conditions, although RANS can also be employed to simulate unsteady flows. In this case, the turbulence is still modelled, but time variation is also included in the equations, increasing the computational time required in comparison to steady RANS [14].

For this work, the $k - \omega$ SST model is used as a baseline. This model behaves as a $k - \varepsilon$ model in the free-stream and as a $k - \omega$ in the near-wall region. The aim is to reduce sensitivity to the inlet values of turbulence ($k - \varepsilon$) as well as improve the near-wall performance ($k - \omega$) [13]. Two additional variations of the $k - \omega$ SST model will be used as well through the project: $k - \omega$ SST with Curvature Correction (CC) and $k - \omega$ SST Scale Adaptive Simulation (SAS).

2.2. Rotation approaches

In a turbomachine, the rotor rotates with a certain speed whereas the stator remains still. The interface between both regions needs to be considered in the simulations, as wakes are produced in the rotor and transported to the stator region [14].

In order to account for the rotation, the fluid domain must be divided into three parts. One part is associated with the rotor, which rotates, and the stator and inlet remain still [15]. The geometry includes 360° for stator and rotor simulating all blades.

The approaches present in this project are: Multiple Reference Frame (MRF) and Sliding Mesh (SM) approach. For the MRF the computational fluid domain remains still so rotation is included in the momentum equations as a source term, whereas for the SM the fluid domain does rotate. RANS simulations are done using MRF for steady simulations and SM for unsteady (URANS). The information is transported between regions using a cyclicAMI interface, in which properties are averaged for each face, with weights defined as the fraction of overlapping areas.

2.2.1. Multiple Reference Frame (MRF)

In this approach the rotor is frozen during the simulation, so the solution obtained corresponds to the instantaneous flow field with the rotor in that specific orientation. The effect of rotor-stator interaction due to the rotation of the impeller is not analyzed due to the lack of mesh motion [16].

To consider rotation in the equations, every cell is assigned a solid body rotation depending on its position in the rotating reference frame and a source term is included in the equations (relative frame of reference is used for fluxes, not so for velocities). This source is the Coriolis (second term in the left hand side of Equation 4) and centrifugal forces (last term in the left hand side of Equation 4) generated by rotation in every cell [14].

$$\operatorname{div}(\mathbf{u}_R \otimes \mathbf{u}_R) + 2\boldsymbol{\Omega} \times \mathbf{u}_R + \boldsymbol{\Omega} \times (\boldsymbol{\Omega} \times \mathbf{r}) = -\operatorname{grad}\left(\frac{p}{\rho}\right) + \nu \operatorname{grad}(\operatorname{div}(\mathbf{u}_R))$$

Equation 4. Momentum equation for incompressible flow in a rotating domain for absolute velocity components in the MRF approach [17].

2.2.2. Sliding mesh

The sliding mesh approach considers the unsteadiness created by the impeller rotation by imposing a relative motion of the rotor region. This gives an improvement of accuracy and an important increase in computational time (it is no longer a steady state simulation) [15]. During the simulations, the mesh moves every time step a certain angle defined by the rotational speed. Therefore, flow properties are transported in a similar way as in the real operating condition, in opposition to the frozen rotor approach [14]. Navier-Stokes equations are solved considering the unsteady terms in the momentum equations (not in continuity, as fluid is treated as incompressible for this case) [14].

3. METHODOLOGY

3.1. Simulation workflow

For any CFD simulation, regardless of the model used, the following steps must be done: pre-processing, solving and post-processing. In each step, the parameter definition and analysis will be different depending if simulations are steady or unsteady. Inside the pre-processing step the mesh must be defined, as well as the set-up in OpenFOAM. The general procedure for the simulations can be seen in Figure 3.

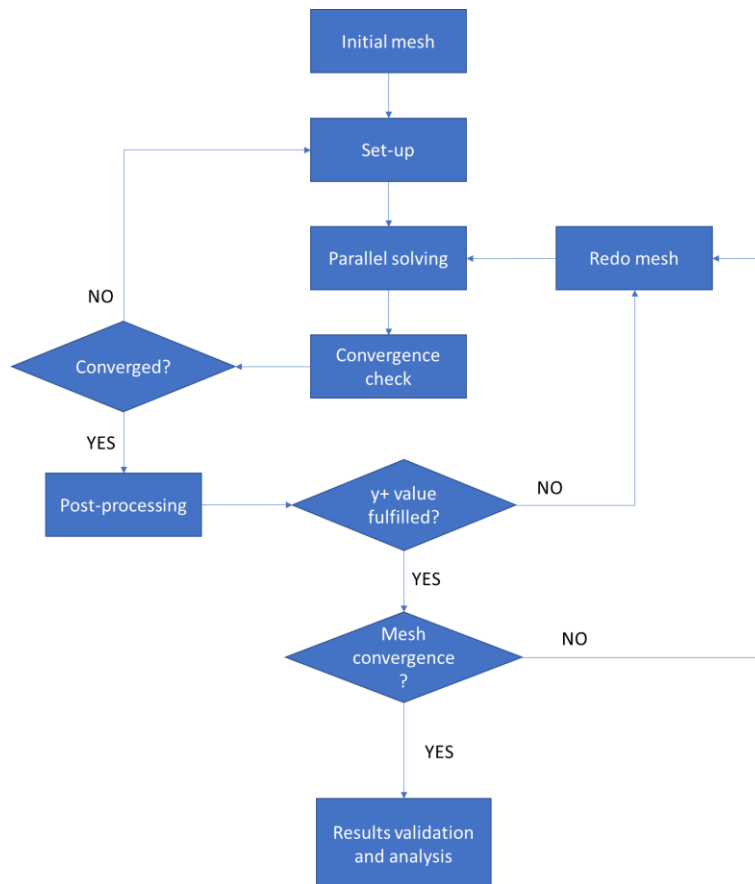


Figure 3. Diagram of general simulation procedure.

All simulations will be done close to the BEP in order to be far away from the cavitation conditions. The first simulations will be a steady RANS with MRF approach. After conducting some parametrical studies in steady-state conditions, the optimum set-up will be defined and used for unsteady RANS simulations with SM mode.

3.2. Geometry

The geometry used for the simulation corresponds to the aluminum rotor model AxWJ-2. This model has some differences in comparison with the rotor geometry used in the experimental test by Li et al. [1]:

A) Blade tip edges on the pressure and suction side of the aluminum model have very small cornering radius. On the contrary, as in the experiment an acrylic rotor was used, there is a higher

3. METHODOLOGY

radius but with unknown value, as it was not reported in the paper. An approximate radius is applied to the aluminum geometry to study the effect of the blade tip shape in the TLV prediction. This parametrical study is presented in section 4.5.

B) The shroud diameter of the aluminum model is the same as in the experiment, but not the tip gap. Due to a misalignment in the experiment, the tip clearance in the measurement plane is 0.9 mm instead of 0.7 mm (value of the CAD geometry) [1]. To fix this difference, the gap clearance of the CAD model was increased by augmenting the shroud diameter in 1.8 mm. Then, all blades have the same tip gap of 0.9 mm. All images shown from simulations, have a different normalization radius than the experimental pictures, i.e. R is equal to 0.153 m instead of 0.1524 m .

3.3. Mesh

The mesh is divided into three zones: stator, rotor and inlet. The stator zone also includes the outlet duct as designed in the experiment [1]. The general dimensions of the geometry can be seen in Figure 4. The length of the inlet duct will be modified in subsequent chapters for parametrical studies. The length used for the final results corresponds to 4D instead of 10D.

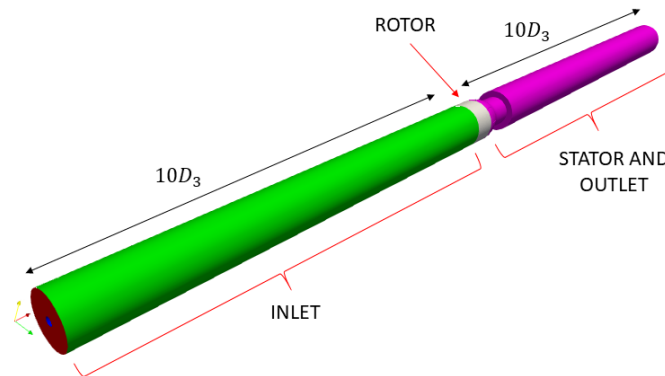


Figure 4. Domain schematic for AxWJ-2.

The mesh is unstructured due to the complexity of the geometry. The near wall region has been meshed using hexahedrons and trying to assure a $y^+ > 30$ to apply wall functions. The region between walls is mainly filled with tetrahedrons, forming the unstructured mesh. Between the three regions (inlet, rotor and stator) a non-conforming mesh is present, as each part has been meshed independently.

In a first approach, three meshes with increasing refinement levels have been used: coarse, medium and fine mesh (Figures 5-7). The fine and medium mesh are obtained from doing a refinement in the rotor region (Figures 6-7). A fourth mesh (refined tip mesh) is created in order to increase mesh resolution in the vortex area by refining the mesh in the tip gap area between the Leading Edge (LE) of the blade and approximately half of its chord length (Figure 8). This procedure was chosen in order to increase accuracy for vortex prediction without increasing too much the computational time of the simulations.

The final size of each mesh can be seen in Table 2.

	Coarse mesh	Medium mesh	Fine mesh	Refined tip mesh
Number of cells in rotor (in millions)	1.94 M	5.07M	12.34 M	24.94 M

Table 2. Number of cells in the rotor region for the meshes used in the project.

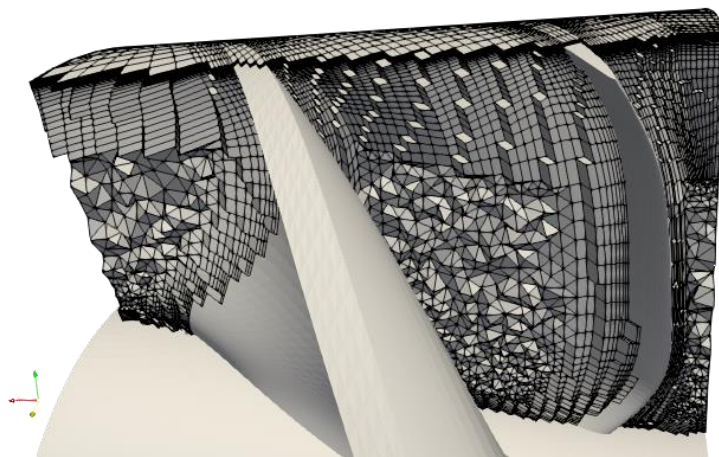


Figure 5. Coarse mesh at the rotor.

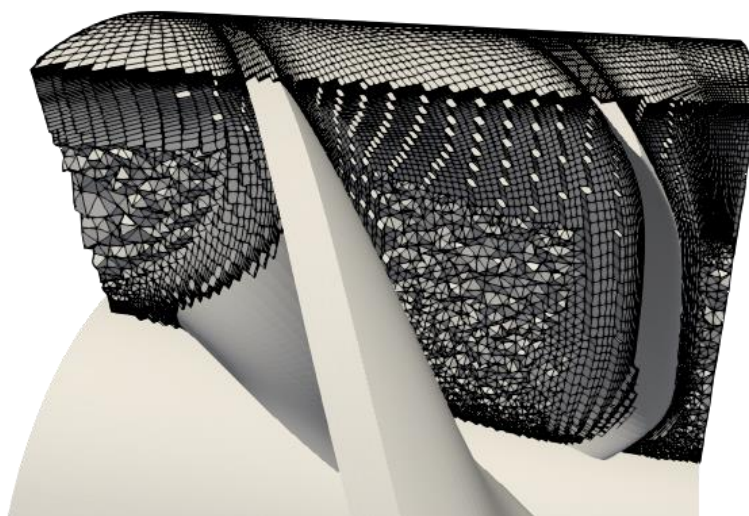


Figure 6. Medium mesh at rotor

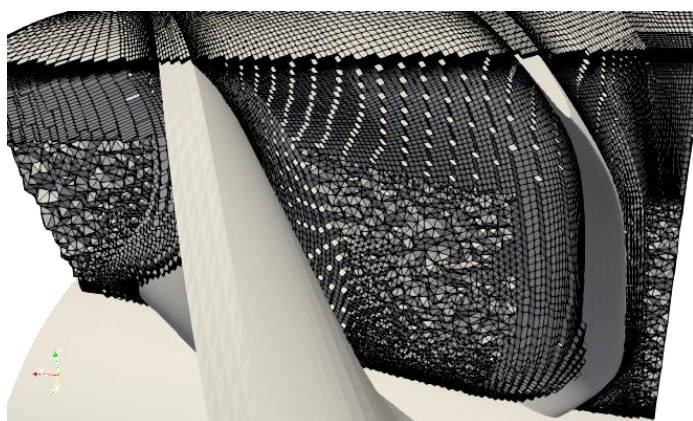


Figure 7. Fine mesh at the rotor.

3. METHODOLOGY



Figure 8. Refined tip mesh to the right and fine mesh to the left at rotor.

3.4. Set-up

In this section, turbulence models, boundary conditions, and other procedures are described. As two different simulations are performed, pre-processing is divided in steady MRF and unsteady SM simulations.

3.4.1. Steady RANS

For setting-up these models, the following conditions are defined:

1. Turbulence model: as mentioned before, the model used as a baseline is the $k - \omega SST$ [18] with wall functions. Also, the $k - \omega SST$ with Curvature Correction (CC) model is tested.
2. Pressure-Velocity coupling: as an incompressible flow is being considered, the SIMPLE algorithm is used. This implies the use of the solver simpleFoam.
3. Linear solvers: the linear solvers can be seen in Table 3.

Parameter	Solver
p	PCG preconditioner GAMG
U.*	PBiCCCG
k	smoothSolver
omega	smoothSolver

Table 3. Summary of solvers used for steady RANS simulations.

4. Schemes: they are chosen in order to increase the stability of the simulation and accuracy (Table 4).

Parameter	Scheme
ddtSchemes	steadyState
gradSchemes	cellLimited Gauss Linear 1
div(phi,U)	Gauss limitedLinearV 1
div(phi,k)	bounded Gauss upwind

div(phi,omega)	bounded Gauss upwind
Laplacian	Gauss linear corrected
Interpolation	Linear

Table 4. Summary of schemes used for steady RANS simulations.

5. Interface: the rotation of the rotor is defined by the MRF approach and a cyclicAMI condition is used for the interface between rotor/stator and rotor/inlet.

6. Boundary conditions:

- *Inlet*: fixed axial velocity will be set for the inlet. For calculating its value, the flow rate of the BEP is used as:

$$Q_{BEP} = \frac{\pi}{4} (D_3^2 - D_{shaft}^2) u_{inlet}$$

where D_3 is the rotor diameter, D_{shaft} is the diameter of the shaft and u_{inlet} the uniform velocity value set at the inlet patch. This results in a value of 4.55 m/s.

Also, the turbulent properties should be set at the inlet, in this case the turbulent kinetic energy k and the specific dissipation ratio ω . The starting point is to assume a turbulent intensity I equal to 5%, so [19]:

$$k = 1.5 (I |u_{inlet}|)^2 = 0.0776 \text{ m}^2/\text{s}^2$$

The turbulent specific dissipation rate is obtained from defining the turbulent viscosity ratio ν_t/ν equal to 10 at the inlet. As the model being used is $k - \omega$ SST, the following equation can be used for estimating the value of ω [20]:

$$\omega = \frac{k}{\nu_t}$$

Therefore, ω should be set to a value of 7054.54 s^{-1} .

The final inlet conditions can be observed in Table 5.

Parameter	Inlet condition
U	(4.55 0 0)
p	zeroGradient
k	type turbulentIntensityKineticEnergyInlet intensity 0.05
omega	type fixedValue value uniform 7054.54
nut	type calculated

Table 5. Summary of inlet conditions for steady RANS simulations.

- *Outlet*: will be set to constant pressure of 55.263. As the flow is incompressible and there is no interest in knowing the real value of the pressure, only the difference between inlet and outlet is obtained. The rest of the parameters are set to zeroGradient, except for k and ω where an inletOutlet condition will be defined with reversed flow values equal to the inlet boundary condition to ease convergence.
- *Wall functions*: wall functions are used like expressed in Table 6.

3. METHODOLOGY

Parameter	Wall function
k	kqRWallFunction - Cmu 0.09 - Kappa 0.41 - E 9.8 - Value uniform 0
omega	omegaWallFunction Same parameters as for k are used.
nut	nutUSpaldingWallFunction Same parameters as before.

Table 6. Summary of wall functions used for steady RANS simulations.

7. Initialization is set to a uniform field equal to the inlet conditions except for pressure, which is set to the outlet value (Table 7). The utility mapFields can also be used to reduce computational time.

Parameter	internalField uniform value
U	(4.55 0 0)
p	55.263
k	0.0776
omega	7054.54
nut	0

Table 7. Summary of initialization values in steady RANS simulations.

8. MRF set-up: only one zone is considered for MRF, the rotor. The excluded patches are shroud wall, rotor-inlet and rotor-stator interfaces. The origin of rotation is located at (0 0 0) along the -X axis with a rotational speed of 94.2 *rad/s* (900 *RPM*).
9. Transport properties: the kinematic viscosity is set to $1.1 \cdot 10^{-6} \text{ m}^2/\text{s}$ and density to 1800 kg/m^3 .

3.4.2. Unsteady RANS

For setting-up this simulation, the following conditions are defined:

1. Turbulence model: the same baseline as for steady RANS will be used and a different variation of the $k - \omega$ SST model is tested: Scale Adaptive Simulation (SAS).
2. Pressure-Velocity coupling: for solving the unsteady equations, the PIMPLE method is used with the solver pimpleDyMFoam (dynamic mesh and unsteady simulation).
3. Solvers: the solvers used can be seen in Table 8.

Parameter	Solver
p	PCG preconditioner GAMG
U.*	PBiCCCG
k	PBiCG
omega	PBiCG

Table 8. Summary of solvers used for unsteady RANS simulations.

4. Schemes: they are chosen in order to increase the stability of the simulation (Table 9).

Parameter	Scheme
ddtSchemes	backward
gradSchemes	cellLimited Gauss Linear 1
div(phi,U)	Gauss limitedLinearV 1
div(phi,k)	Gauss upwind
div(phi,omega)	Gauss upwind
Laplacian	Gauss linear limited corrected 0.1
Interpolation	Linear limited corrected 0.1

Table 9. Summary of schemes used for unsteady RANS simulations.

5. Interface: the rotation of the rotor is defined by the sliding mesh model and a cyclicAMI condition is used for the interface between rotor/stator and rotor/inlet.
6. Boundary conditions: all boundary conditions will be the same as for the steady simulation.
7. Sliding mesh set-up: The definition of the motion is set in the dynamicMeshDict as follows:

Keyword	Definition
dynamicFvMesh	dynamicMotionSolverFvMesh
motionSolver	solidBody
solidBodyMotionFunction	rotatingMotion

Table 10. Set-up of the dynamicMeshDict for unsteady RANS simulations.

8. Transport properties: same as for steady simulation.

3.4.3. Summary

A summary of the main aspects to consider for steady and unsteady simulations can be seen in Table 11.

3. METHODOLOGY

Comparison between	Steady RANS	Unsteady RANS
<i>Turbulence model</i>	<i>k – ω SST</i>	<i>k – ω SST</i>
<i>Pressure-Velocity coupling</i>	SIMPLE	PIMPLE
<i>Rotor motion approach</i>	MRF	Sliding mesh
<i>Rotor/stator and Rotor/Inlet interface</i>	cyclicAMI	cyclicAMI
<i>Solver</i>	simpleFoam	pimpleDyMFoam
<i>Schemes</i>	limitedLinear	limitedLinear
<i>Near wall approach</i>	Wall functions	Wall functions

Table 11. Summary of the set-up of the simulations

4. STEADY RANS SIMULATIONS

The main purpose of steady RANS simulations is to perform several parametrical studies in order to analyze the effect on the TLV structure and obtain the most adequate set-up for future simulations. The results obtained will be validated with the SPIV data from Li et al [1].

4.1. Validation of results

4.1.1. Performance prediction

From the experimental performance curve in Tan et al [10], a reference flow coefficient φ_{ref} (equal to 0.76) and the corresponding head rise coefficient ψ_{ref} (which is 2.516) are known.

For the meshes studied:

	ψ/ψ_{ref}	φ / φ_{ref}	η predicted
Coarse mesh	1.00	1.00	85.8%
Medium mesh	1.00	1.01	87.4%
Fine mesh	0.98	1.00	85.8%
Refined tip mesh	0.99	1.00	85.9%

Table 12. Performance validation for steady RANS simulations.

The error stays within 2% margin for the head coefficient, 1% for the flow coefficient and the predicted efficiency remains approximately constant, except for the medium mesh. This discrepancy could be due to the slight increase in flow rate for the medium mesh case. In addition, a grid convergence study will be performed in section 4.6.

4.1.2. TLV structures

For validating the TLV structures, the results are compared with the SPIV measurements shown in Li et. al [1]. All the measurement planes are meridional and located in the tip region, showing the SS of the blade. An example of the planes' location can be seen in Figure 9 as a red line at the rotor region.

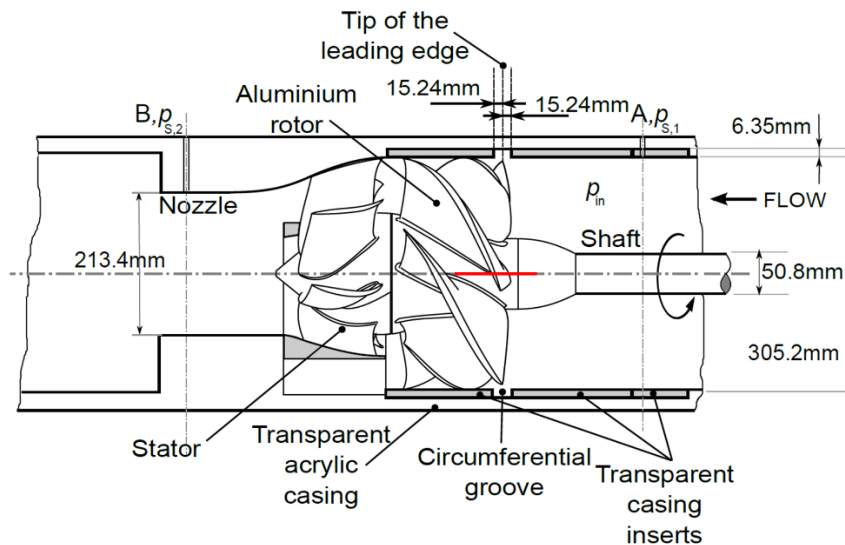


Figure 9. Sketch of the plane location at the pump [21].

4. STEADY RANS SIMULATIONS

These planes are located at different positions along the blade chord length in order to analyze the development of the TLV. To locate the planes, they are named in terms of the parameter s/c , being s a linear coordinate along the tip chord c . Figure 10 shows the location of the planes and the nomenclature that is used in the thesis.

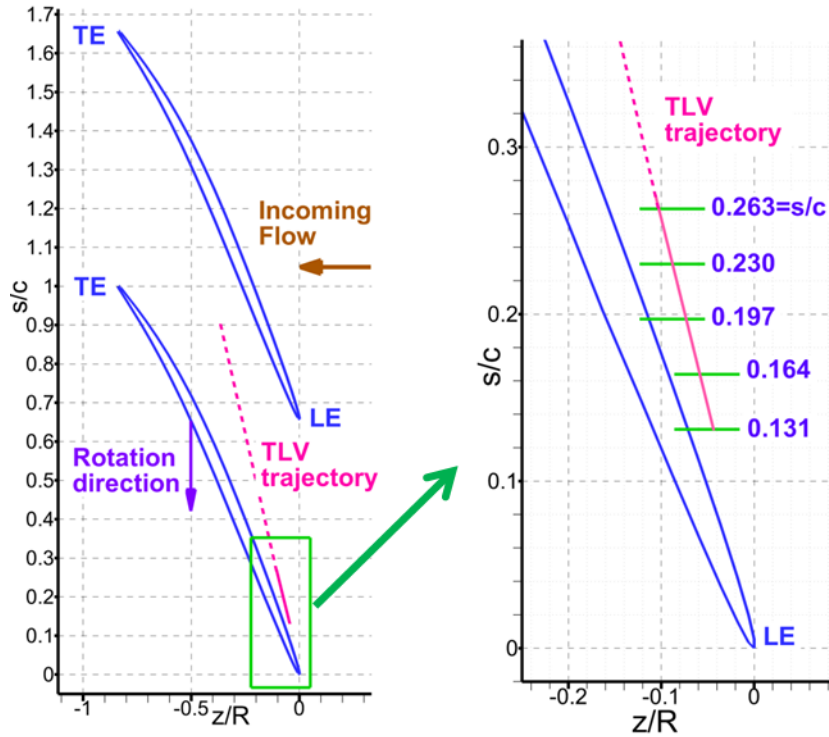


Figure 10. SPIV planes location used in the experiment in Li et. al [21]

The results shown in this section correspond to the 1st fillet case (explained in section 4.5), where the geometry is modified in order to obtain better agreement with experiments. The inlet duct length is $4D$ with uniform inlet velocity, $k-\omega$ SST model and tip refined mesh are used (Figure 8). As the results are steady state, they are compared to the averaged values measured during the experiment as no instantaneous values are available from this simulation. Result's comparison between the experiment and simulations can be seen in Figure 11-13, presented in an absolute frame of reference. Figures 11 and 12 show good agreement with experiment although the vortex core is located slightly closer to the shroud wall and blade than the experimental data. However, Figure 13 shows much lower values for the turbulent kinetic energy from simulations as the TKE is obtained from the turbulence modelling and not from resolved turbulence.

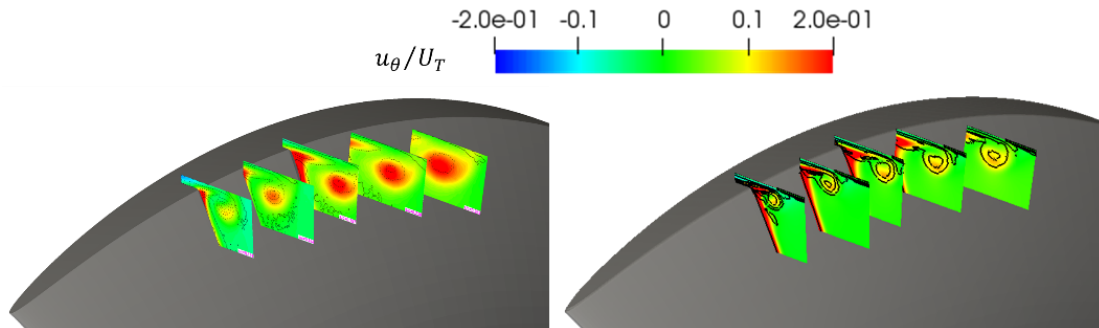


Figure 11. U_θ/U_T distribution and ω_θ isolines for each measurement plane, where the left figure corresponds to the experiment [1] and the right one to MRF 1st fillet case.

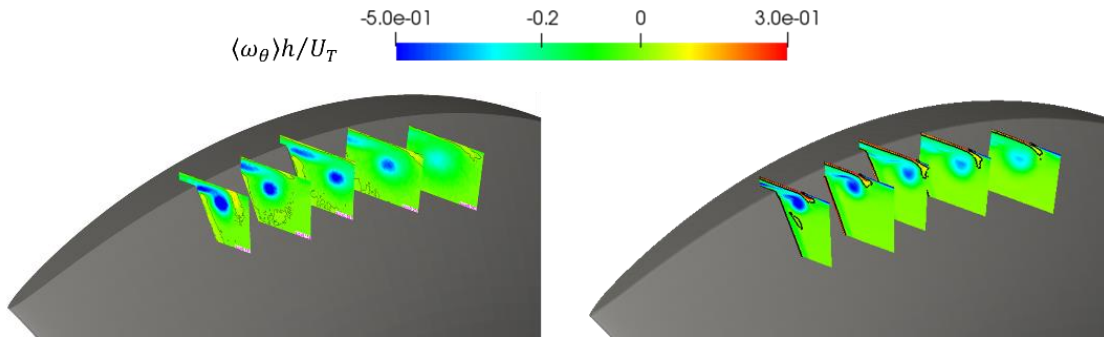


Figure 12. $\omega_\theta h / U_T$ distribution and $\omega_\theta = 0$ isolines for each measurement plane, where the left figure corresponds to the experiment [1] and the right one to MRF 1st fillet case..

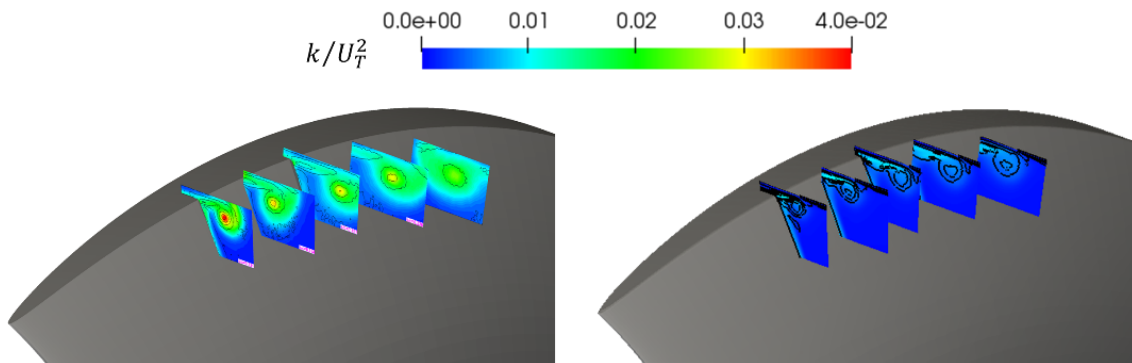


Figure 13. k / U_T^2 distribution and ω_θ isolines for each measurement plane, where the left figure corresponds to the experiment [1] and the right one to MRF 1st fillet case..

As explained in Li et al [1], there are three main structures in the tip region (Figure 14-b): TLV center (A), shear layer (B) and the endwall boundary layer separation (C). For analyzing these structures, the first plane is studied in depth (Figure 14 and 16).

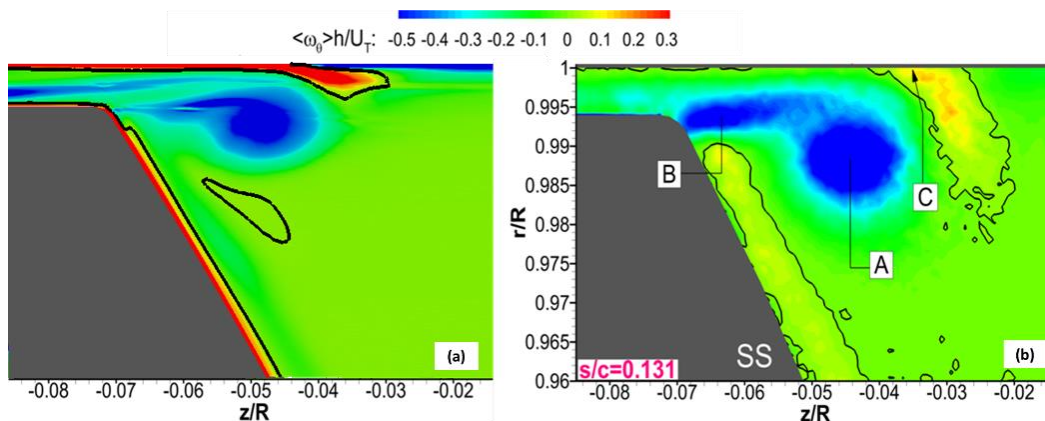


Figure 14. $\omega_\theta h / U_T$ distribution and $\omega_\theta = 0$ isolines in the plane $s/c = 0.131$ with: a) simulation for the 1st fillet case and b) experimental results [1].

From Figure 14-a, it can be seen a region with high negative vorticity close to the blade tip. This region corresponds to a recirculation bubble created in the tip gap. Flow surrounding the PS of the blade close to the gap is ‘pushed’ into the gap because of the pressure difference between PS and SS, following the blade surface (Figure 15, vectors are scaled for visualization purposes). When it gets to the edge, the flow detaches from the blade surface after the edge and this creates a separation region close to the tip surface. A bigger recirculation region reduces the tip leakage flow rate that gets to the TLV structure on the SS of the blade, thus reducing its strength and moving it closer to the blade edge. Consequently, the smoother the edge geometry in the PS of the blade, the smaller the separation region (and higher flow rate), changing the shape and location of the TLV (as explained in section 4.5).

4. STEADY RANS SIMULATIONS

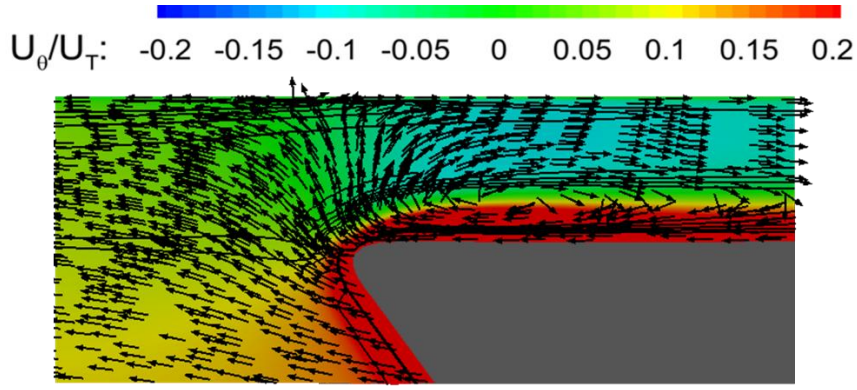


Figure 15. U_θ/U_T distribution and ω_θ isolines in the plane $s/c = 0.131$ on the PS of the blade for 1st fillet case.

From tangential velocity contours in Figure 16, the TLV center is predicted with higher tangential velocity and is located closer to the SS of the blade and the shroud wall. This discrepancy is proved to be highly affected by the blade shape (section 4.5). Therefore, as the experimental radius is not provided, it is not possible to fully reproduce the experimental set-up. The blade shape also has an important impact in the shear layer (B) however not so for the boundary layer separation (C).

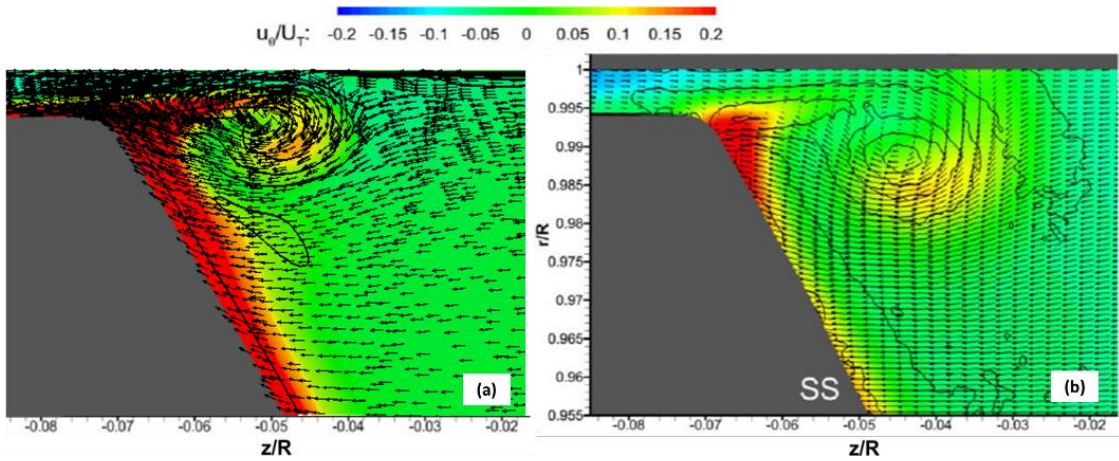


Figure 16. U_θ/U_T distribution, ω_θ isolines and scaled vectors in the plane $s/c = 0.131$ with: a) simulation results for the 1st fillet case and b) experimental results [1].

Another visible difference between simulation and experiment in Figure 16 is the boundary layer resolution close to the walls, both in the blade and the shroud. From JHU, it was declared that the resolution of the SPIV measurements was not adequate for resolving so close to the wall. Then, the high tangential velocity present close to the walls is lowered when averaging over an interrogation window that covers a wide area near the blade wall. On the contrary, the simulation provides good resolution close to the wall, providing higher values of tangential velocity close to the blade walls.

4.2. Sensitivity analysis

4.2.1. Boundary layer thickness

Boundary conditions must resemble the test conditions of the experiment in order to compare the results. The velocity profile upstream of the rotor inlet is available, given by the Laboratory for Experimental Fluid Dynamics of JHU. The plane is located at a position of $z/R = 0.65$ where z is the axial coordinate in the cylindrical frame and R is the rotor diameter.

In this analysis, five different inlet duct lengths are analyzed, which provide different BL

thicknesses close to the tip region. These lengths are: four, six, eight and ten times the diameter of the pump. These four cases are compared in terms of the following aspects:

A) Velocity profile at the rotor inlet

The axial velocity (in cylindrical coordinates, U_z) is extracted at a position of $z/R = 0.65$ upstream of the rotor inlet as shown in Figure 17. It can be observed that the shorter the inlet duct, the closer it gets to the experimental measurements in the shroud wall region. Velocity profile close to the hub has less impact on the TLV structures, so a big difference between experiment and simulations in that region should not highly influence TLV.

However, it should be mentioned that Figure 17 shows the velocity profiles normalized by the mean velocity of each case. This is to compare the shape of the profile without considering possible differences in flow rate. Actually, the experiment has a flow rate deviation of approximately 5% over the BEP whereas the performed simulations are 2% below it.

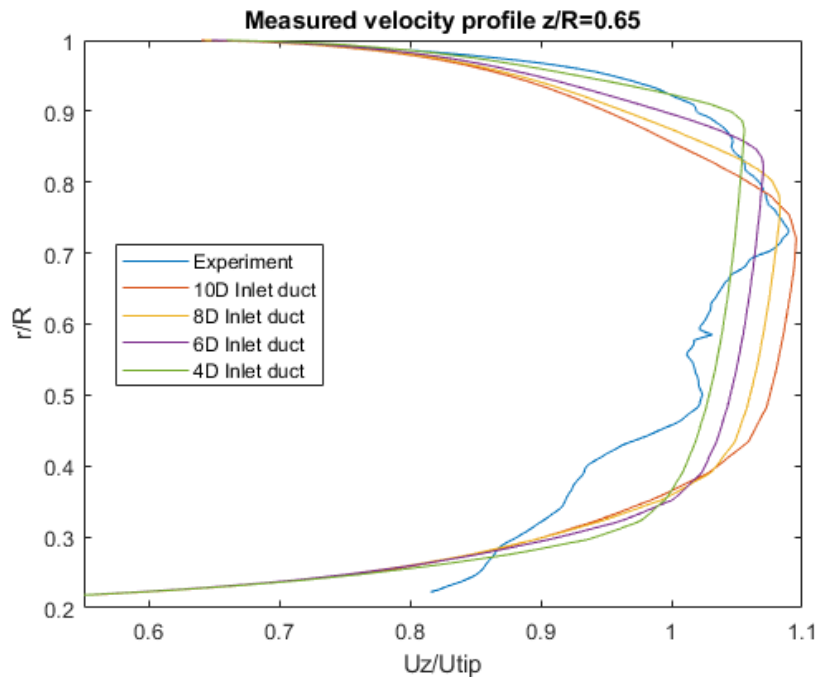


Figure 17. Inlet velocity profile at $z/R = 0.65$ upstream of rotor for experiment and different inlet duct's length.

A different profile in the tip region will mean different momentum rate in the boundary layer, influencing the formation and evolution of the TLV and the endwall boundary layer separation. Looking closer at that region (Figure 18), still a big difference can be observed between simulations and experiment. A possible solution to this difference in the profile shape is to impose the experimental velocity profile at the inlet boundary condition of the 4D inlet case, as it is the closest to the experimental profile. This is analyzed in section 4.2.2.

4. STEADY RANS SIMULATIONS

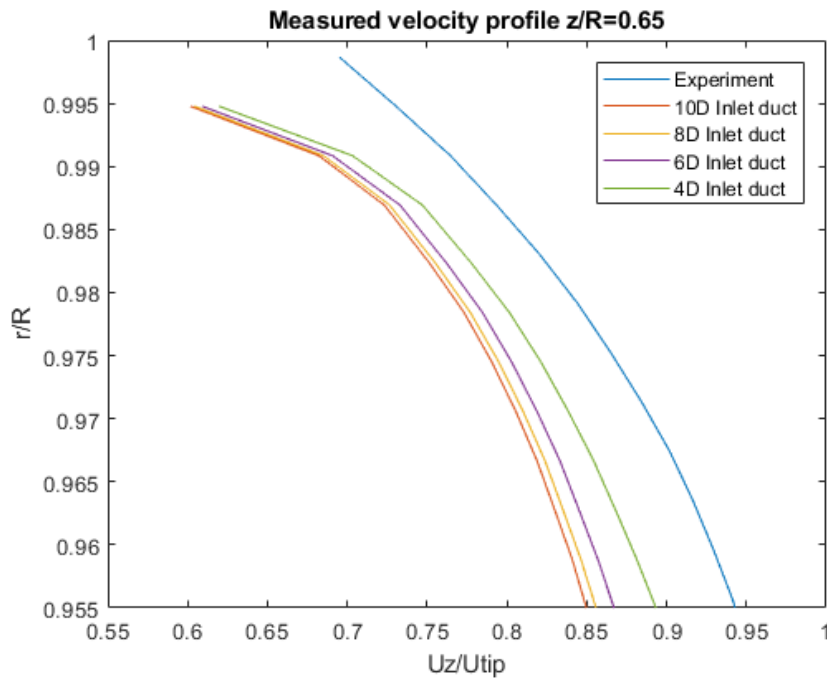


Figure 18. Detail of the velocity profile in the tip region for different duct lengths.

B) Performance prediction

The head rise is studied for the four cases in Figure 19. No big difference can be observed in terms of performance prediction for each length analyzed.

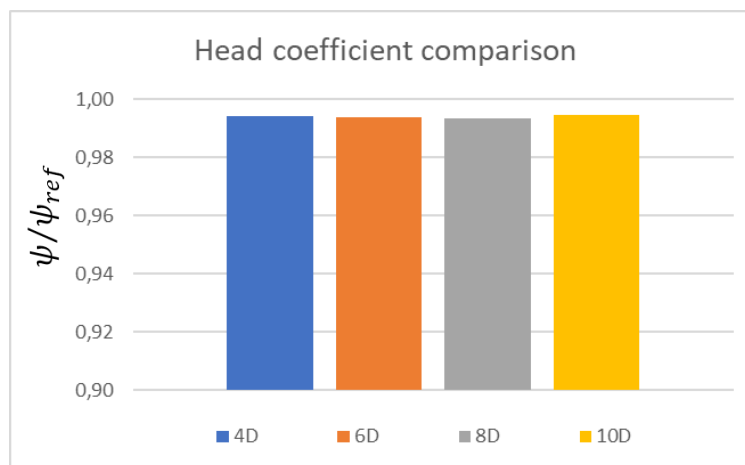


Figure 19. Head coefficient comparison for different inlet lengths.

C) TLV trajectory comparison

For analyzing the TLV shape and trajectory, the Q criterion is used for the first four cases (Figure 20). A difference in the boundary layer thickness doesn't highly influence the shape and trajectory of the TLV starting from a plug flow at inlet.

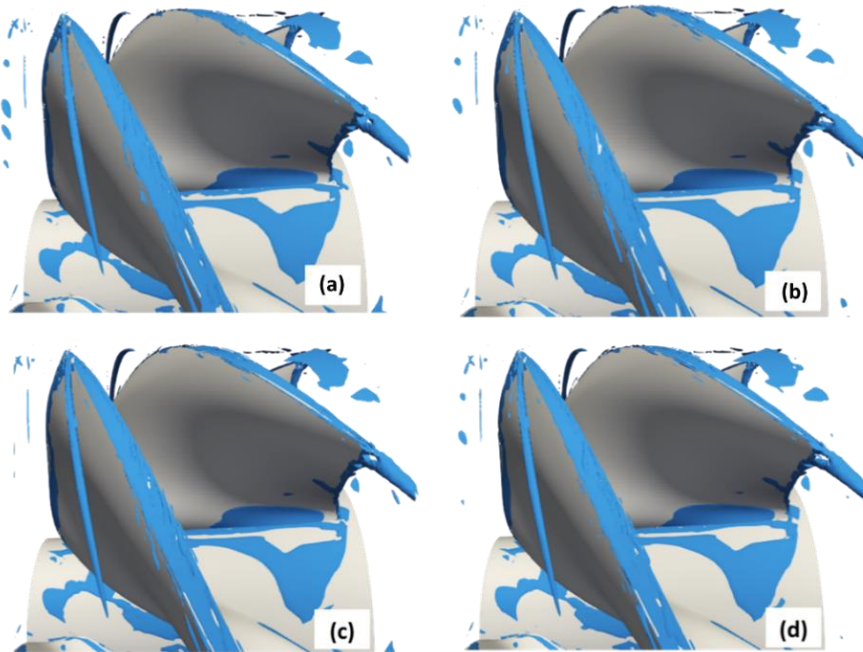


Figure 20. Q criterion plots for: a) 4D, b) 6D, c) 8D and d) 10D case.

D) TLV experimental planes comparison

Due to the similarity of the TLV trajectories, no big difference is expected either for the Stereoscopic Particle Image Velocimetry (SPIV) planes comparison. The first and last plane are analyzed for the two extreme cases: 10D and 4D. From Figure 21 and 22, no remarkable difference can be seen between both cases.

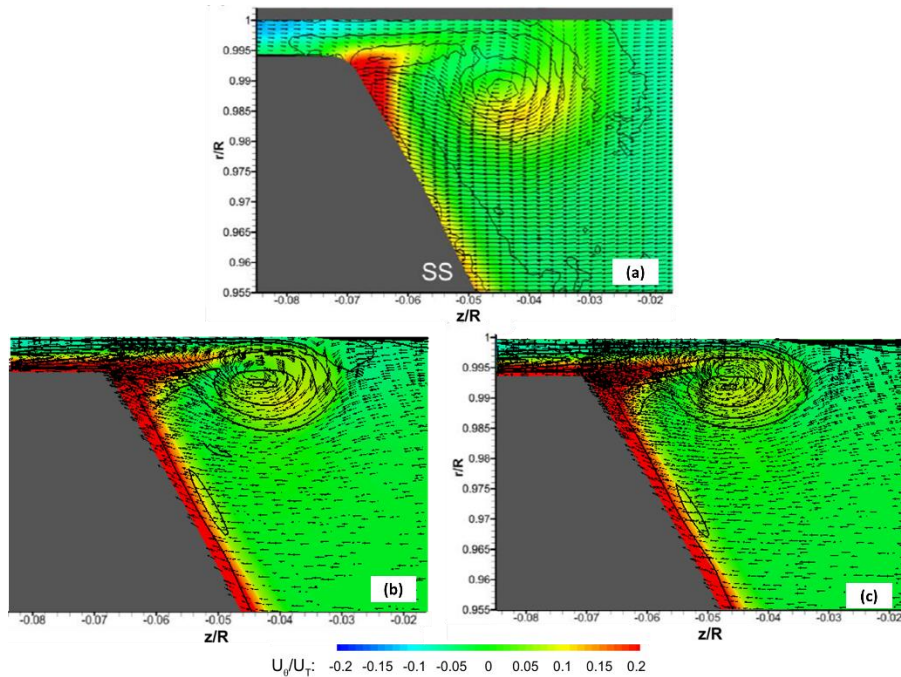


Figure 21. U_θ/U_T distribution, ω_θ isolines and scaled vectors in the plane $s/c = 0.131$ with: a) experimental result [1], b) 10D case and c) 4D case.

4. STEADY RANS SIMULATIONS

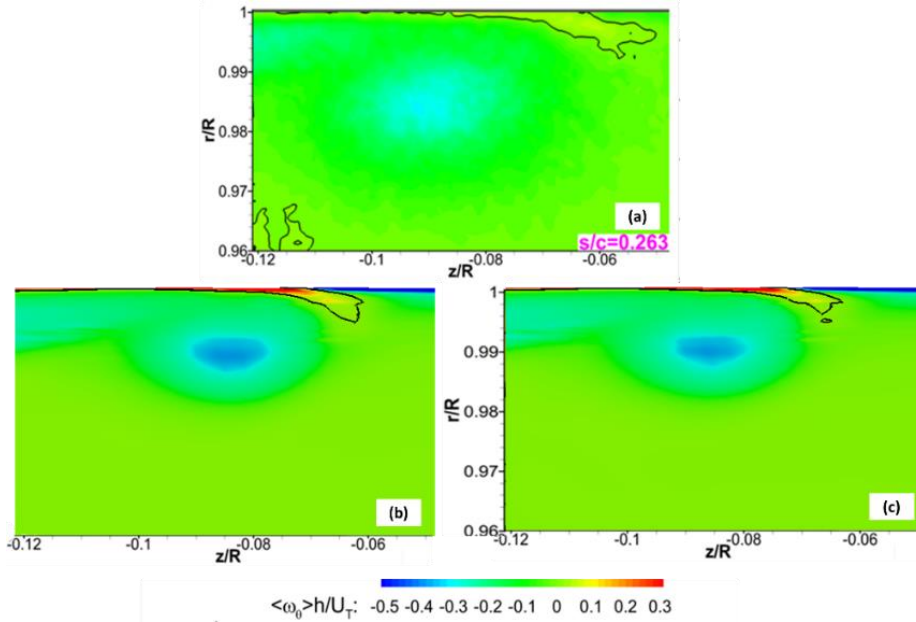


Figure 22. $\omega_\theta h / U_T$ distribution and $\omega_\theta = 0$ isolines in the plane $s/c = 0.263$ with: a) Experimental result [1], b) 10D case and c) 4D case.

For studying the cause of this similitude, the velocity profile is analyzed at different sections before the blade LE (Figure 23) for the extreme cases: 4D and 10D inlet duct length. The difference in velocity between these two cases is not very significant, even smaller the closer to the shroud wall.

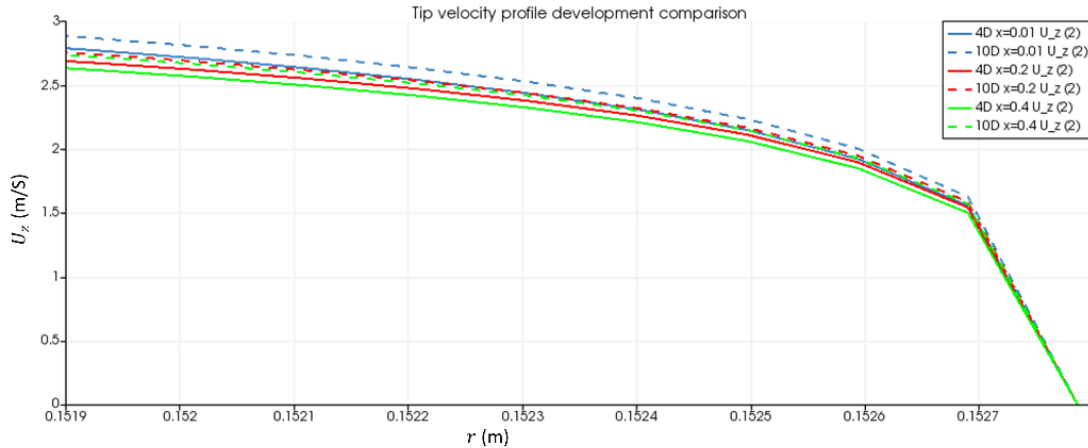


Figure 23. Axial velocity profile in the tip region at further sections from the blade LE for 4D and 10D case, where x is the axial coordinate.

Furthermore, the flow rate and velocity profile in the first measurement plane ($s/c = 0.131$) is studied. Two lines are used to measure the velocity profile at the tip gap (white line at the left) and the inlet (white line at the right) as shown in Figure 24. The velocity profiles can be seen for each case in Figure 25, where the inlet velocity is shown only for the tip gap length range. No clear relation between the profiles can be extracted from it, so a further analysis concerning flow rate values is performed.

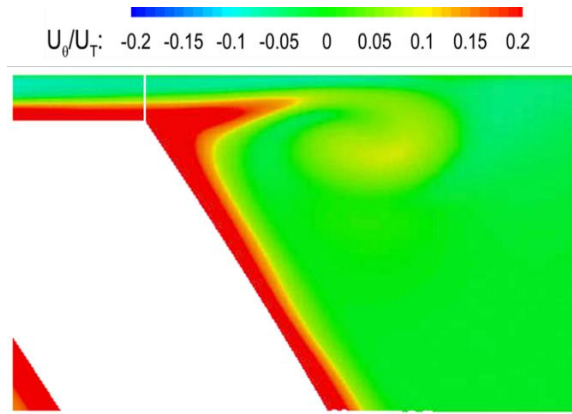


Figure 24. Lines where velocity profile will be measured in $s/c = 0.131$ with U_θ/U_T distribution.

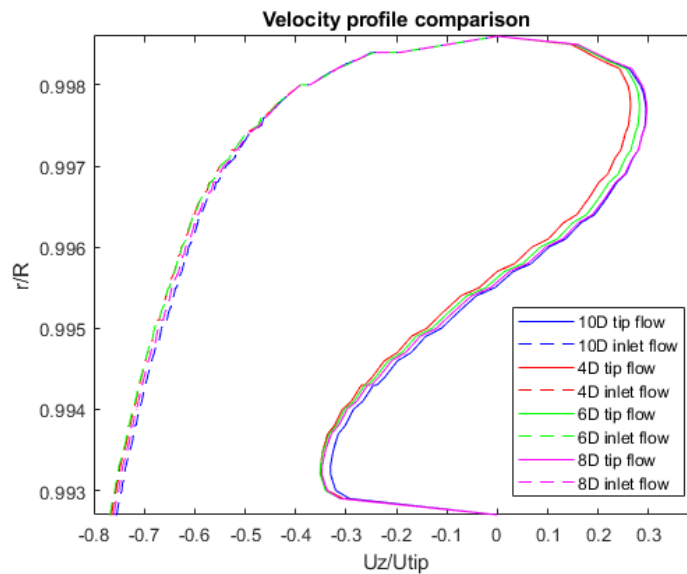


Figure 25. Velocity profiles at tip gap and inlet at the plane $s/c = 0.131$ for different inlet duct's lengths.

In order to calculate the flow rate at both lines seen in Figure 24, the mean velocity between two consecutive radial points is multiplied by the area of the annulus formed between those points. The sum of all the contributions generates the total flow rate in m^3/s . From Figure 26, no clear trend can be extracted. However, the difference in flow rate between 4D and 10D cases are barely 10%. This, together with previous analysis regarding velocity profiles, explains the similitude in results.

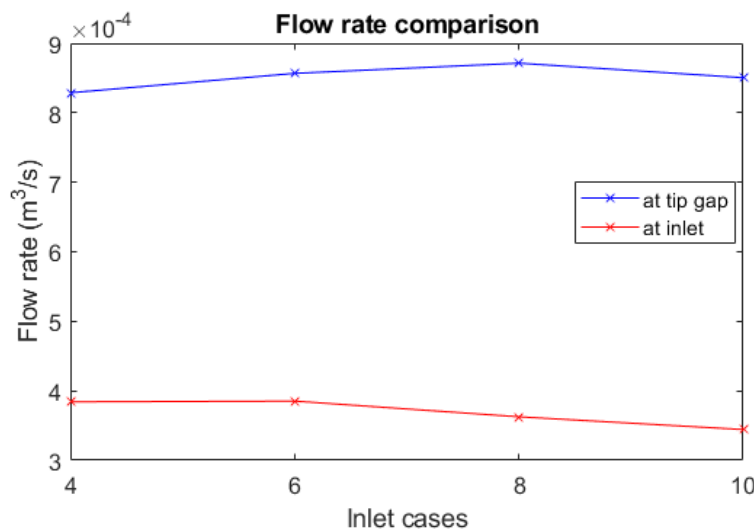


Figure 26. Flow rate analysis at inlet and tip gap at plane $s/c = 0.131$ for different BL thickness cases.

4. STEADY RANS SIMULATIONS

4.2.2. Inlet velocity profile

All cases present in section 4.2.1. have a uniform velocity profile at the inlet. In this section, the velocity profile set at the inlet patch is the experimental profile shown in Figure 27. The case used for comparison in this study is the 4D inlet duct's length case as it is the closest case to the experimental set-up (regarding velocity profiles).

For setting the experimental velocity profile at the inlet, an approximate polynomial function dependent on the variable r/R is obtained. After obtaining the coefficients of a six-order polynomial, an OpenFOAM utility is created. In this utility, the axial component of velocity is replaced by this polynomial equation. For assuring the same flow rate as in the other simulations, a correction coefficient is defined. It is equal to the flow rate needed divided by the actual flow rate of the profile imposed. After calculating the flow rate, the correction factor can be applied and the final profile set.

Two different cases are considered. In the first one, the experimental profile is set at the 4D inlet patch maintaining the same set-up as before (named as '4D no-slip' case). In the second one, a slip condition will be set to all walls in the inlet duct until the measurement plane, where no-slip conditions are stated as usual (named as '4D slip' case). Again, the following aspects will be studied:

A) Velocity profile at inlet

From Figure 27, it can be concluded that the 4D slip case resembles better (in overall) the experimental profile at the measurement plane. Nevertheless, there has been an acceleration close to the shroud and a deceleration close to the shaft walls. This may be due to the contraction of the flow when it reaches the shaft's diameter expansion. This acceleration close to the shroud wall will highly influence the BL in the tip region and consequently, the TLV structure (Figure 28). The velocity close to the tip region is slightly higher than the experimental profile, increasing the kinetic energy within the BL.

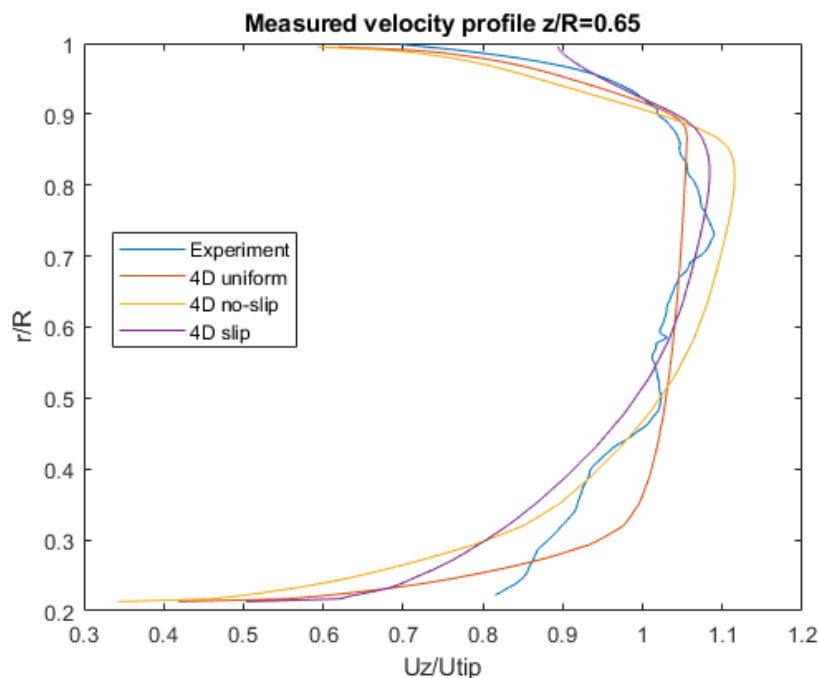


Figure 27. Inlet velocity profile at $z/R = 0.65$ upstream of rotor for experiment, 4D uniform velocity profile and experimental profile.

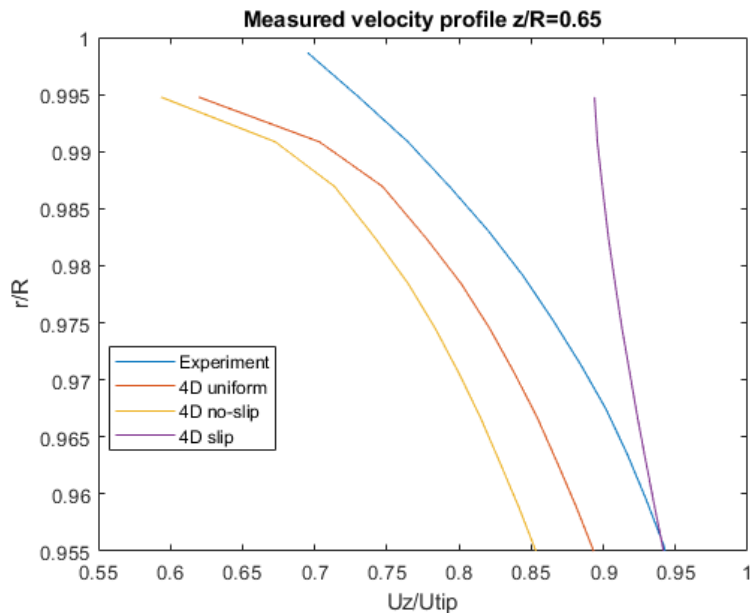


Figure 28. Detail of the velocity profile close to the shroud walls for experiment, 4D uniform velocity profile and experimental profile.

A possible solution would be to know how the velocity profile is in the experiment where there is no contraction of the area, i.e. before the expansion of the shaft. Then, that profile could be set at the inlet and maintained until the new measurement plane by using the slip condition. Unfortunately, this data is not available.

B) Performance prediction

The three cases are set for the same flow coefficient, so the same performance prediction should be expected. This can be seen in Figure 29.

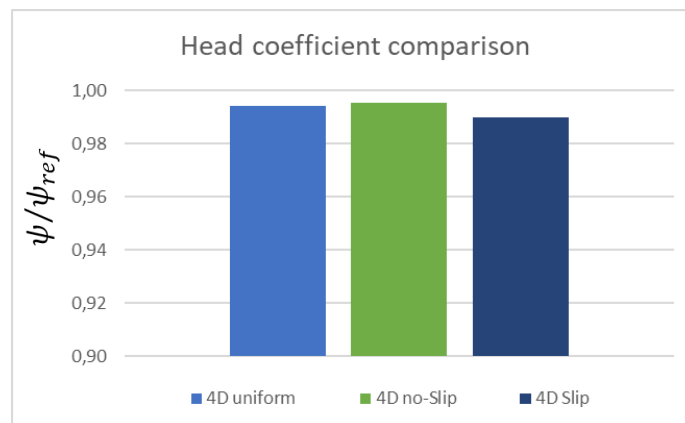


Figure 29. Head coefficient comparison for uniform and experimental velocity profile at a 4D inlet duct.

C) TLV trajectory comparison

All cases seem to be very similar except for the TLV of the ‘4D slip’ case, which is slightly closer to the blade edge (Figure 30). This will be seen as well on the SPIV planes.

4. STEADY RANS SIMULATIONS

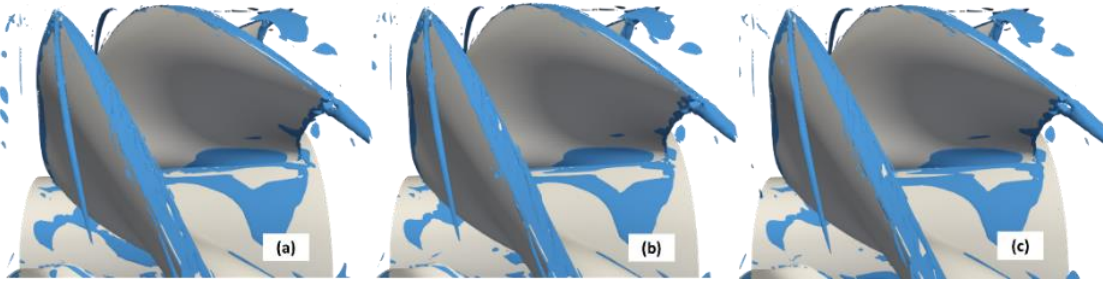


Figure 30. Q criterion plots for a 4D inlet duct with a) uniform velocity, b) 4D no-slip case and c) 4D slip case.

D) TLV experimental planes comparison

Looking at Figure 31 in the 4D slip case, the TLV structure is closer to the edge of the SS of the blade. Also, it has slightly higher tangential velocity values compared to the other cases which can be a consequence of the higher kinetic energy at the BL. Consequently, from Figures 31 and 32, it can be concluded that the no-slip and uniform cases seem more feasible for correctly predicting TLV structures.

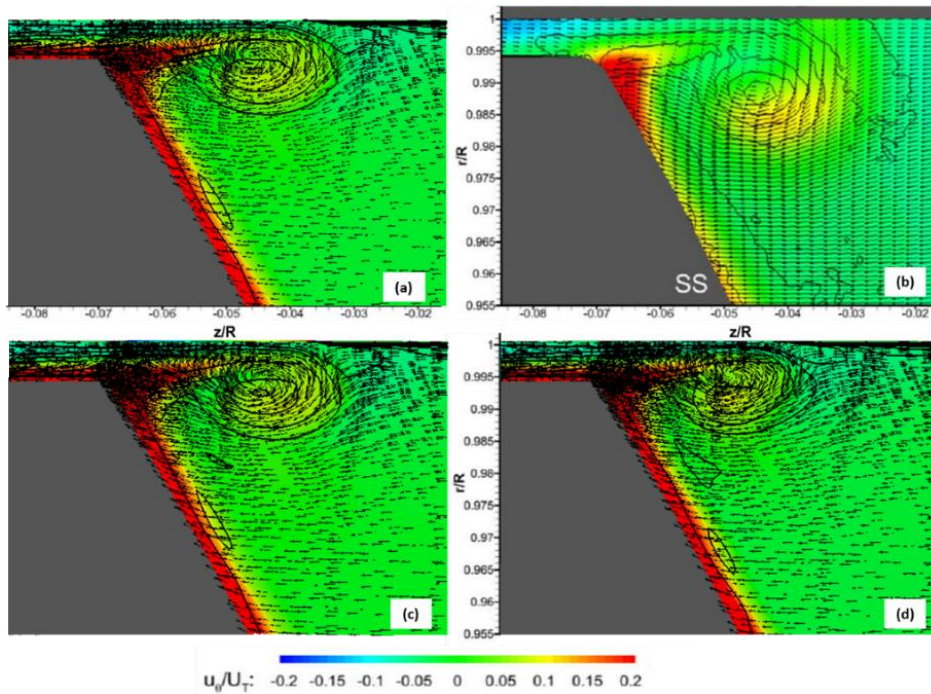


Figure 31. U_θ/U_T distribution, ω_θ isolines and scaled vectors in the plane $s/c = 0.131$ with: a) 4D uniform case, b) experimental result [1], c) 4D no-slip and d) 4D slip case.

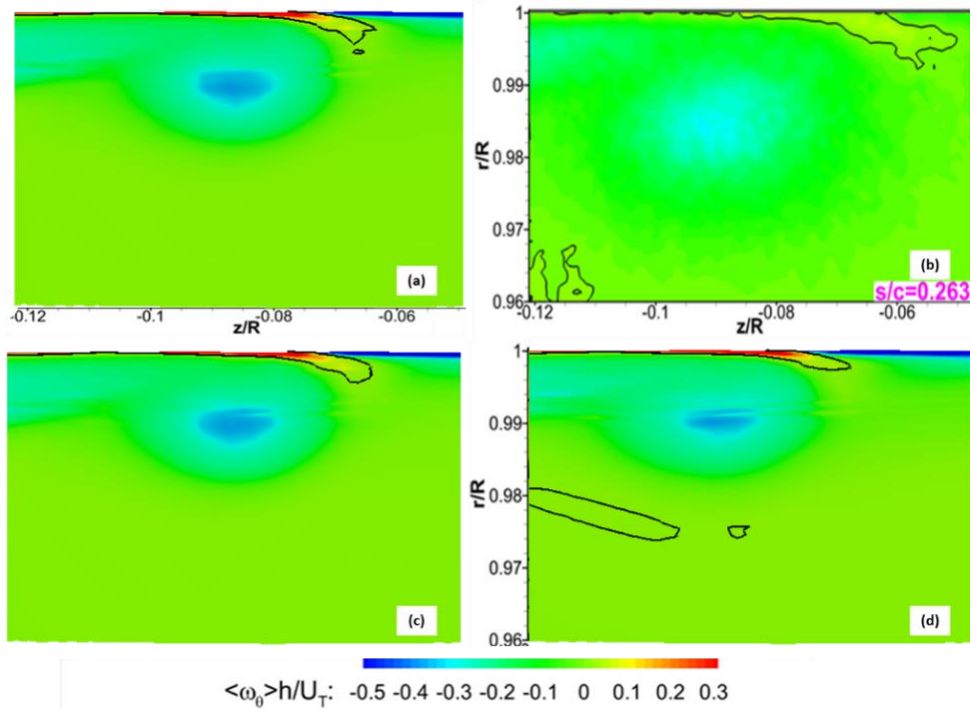


Figure 32. $\omega_\theta h/U_T$ distribution and $\omega_\theta = 0$ isolines in the plane $s/c = 0.263$ with: a) 4D uniform, b) experimental result [1], c) 4D no-slip and d) 4D slip case.

Finally, the criteria for selecting one of the cases as the optimal set-up will be the velocity profile at the measurement plane, as there is clear difference between cases (Figure 28). Then, the closest case to the experiment in the tip region is the uniform inlet case. This case is also easier to reproduce for future simulations.

4.2.3. Turbulence model

To study the turbulence model sensitivity, a simulation is done using the model $k - \omega$ SST with Curvature Correction (CC). This new model aims to account for rotation in the flow streamlines by correcting the production term in the turbulence parameters [22]. Simulations are performed with a uniform inlet velocity profile for a 10D inlet duct. Still, these results can be extrapolated to other inlet ducts' lengths as mentioned in the report.

The results of CC model for MRF show strong unsteadiness. One possible solution that shouldn't differ much from solving an unsteady case and averaging over time, is to average over a specific number of iterations. To calculate this number of iterations, the axial force parameter results are used, calculated on the rotor blades and hub. Several averages are done for the force parameter in groups of 2000 iterations, this is: 2000, 4000, 6000 and so on. When the mean value does not change significantly from one group to the following, that number of iterations is chosen for field averaging.

In the first SPIV plane (Figure 33), the CC model estimates higher diffusion of the TLV while transporting it closer to the core flow. This directly affects the formation of the endwall boundary layer separation, as the space between the TLV core and the shroud wall is minimized. On the other hand, the TLV looks more defined in the last plane for the CC model and still its location is shifted (Figure 34). The CC turbulence model seems less adequate for the purpose of the project.

4. STEADY RANS SIMULATIONS

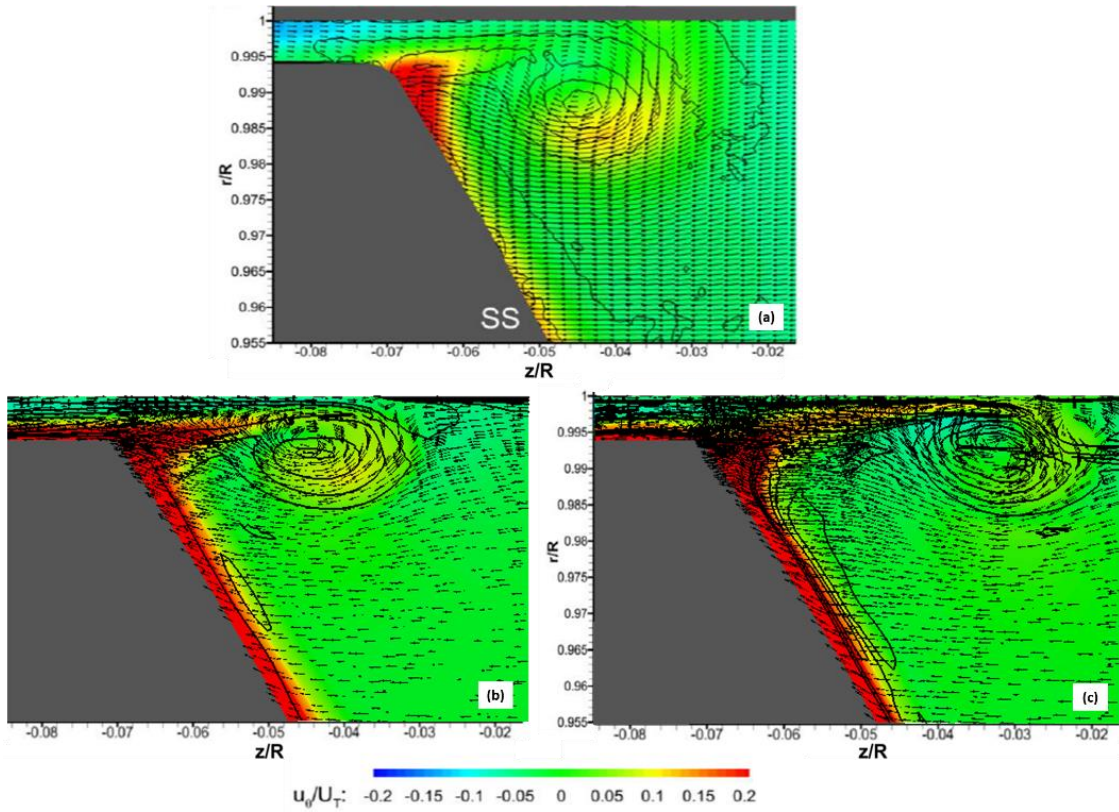


Figure 33. U_θ/U_T distribution, ω_θ isolines and scaled vectors in the plane $s/c = 0.131$ with: a) Experimental result [1], b) $k - \omega$ SST and c) $k - \omega$ SST CC case.

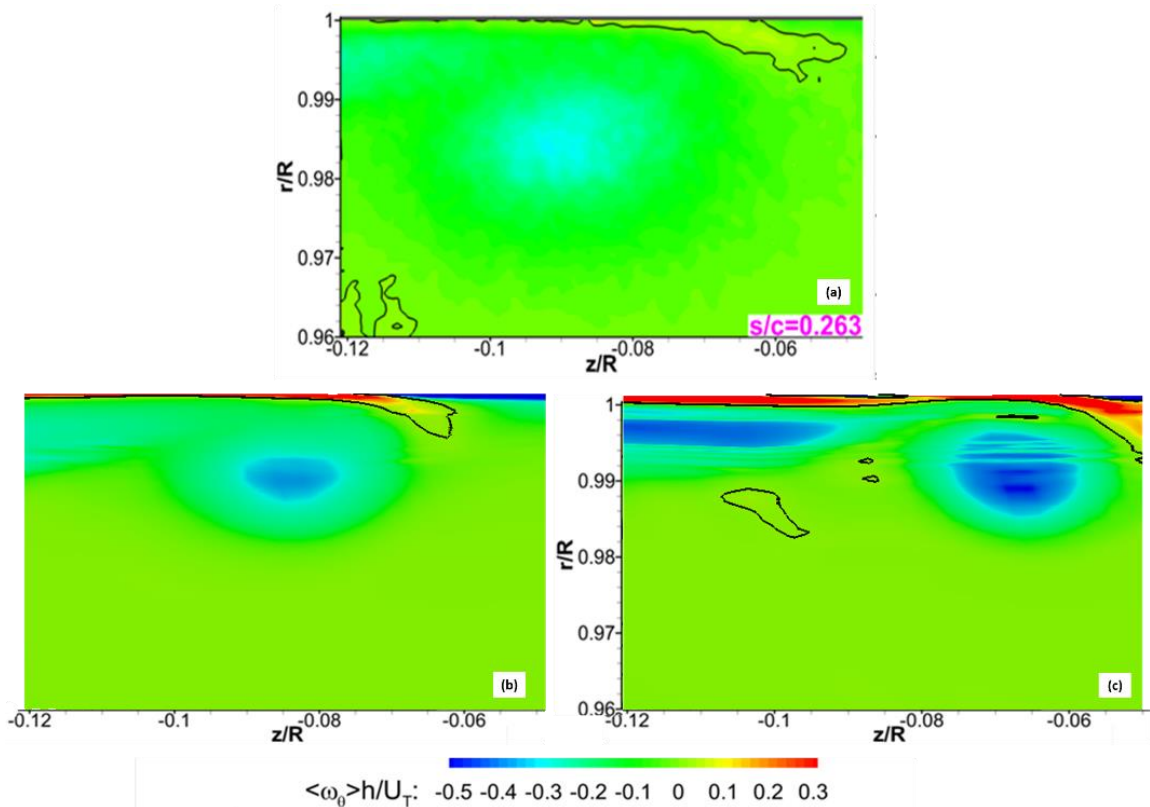


Figure 34. $\langle \omega_0 \rangle h/U_T$ distribution and $\omega_\theta = 0$ isolines in the plane $s/c = 0.263$ with: a) Experimental result [1], b) $k - \omega$ SST and c) $k - \omega$ SST CC case.

4.2.4. Mesh refinement

Four levels of refinement are studied: coarse (Figure 5), medium (Figure 6), fine (Figure 7) and refined tip mesh (Figure 8). The results shown are for $k - \omega$ SST model and an inlet duct of $10D$ with uniform velocity profile except for the medium mesh, which is performed for a $4D$ inlet duct length. However, as explained in section 4.2.1, the results are hardly affected by the BL thickness, so comparison is still possible between $10D$ and $4D$ inlet cases.

First, performance prediction is analysed in Figure 35. Notably increasing the number of cells to better resolve the fluid domain at the rotor does not highly influence the performance. However, a grid convergence study is conducted in section 4.6.

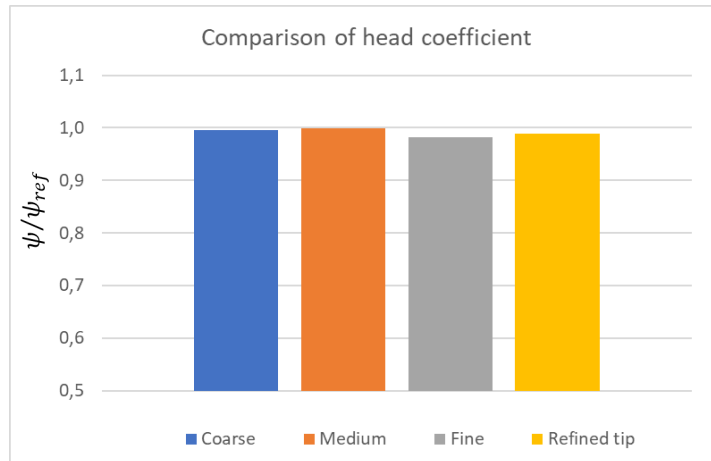


Figure 35. Head coefficient comparison for different mesh size.

A finer mesh in the tip region provides better resolution of the TLV. This effect can be observed in Figure 36 d), which provides a closer result to the experiment, whereas for the coarse mesh the TLV is not even present.

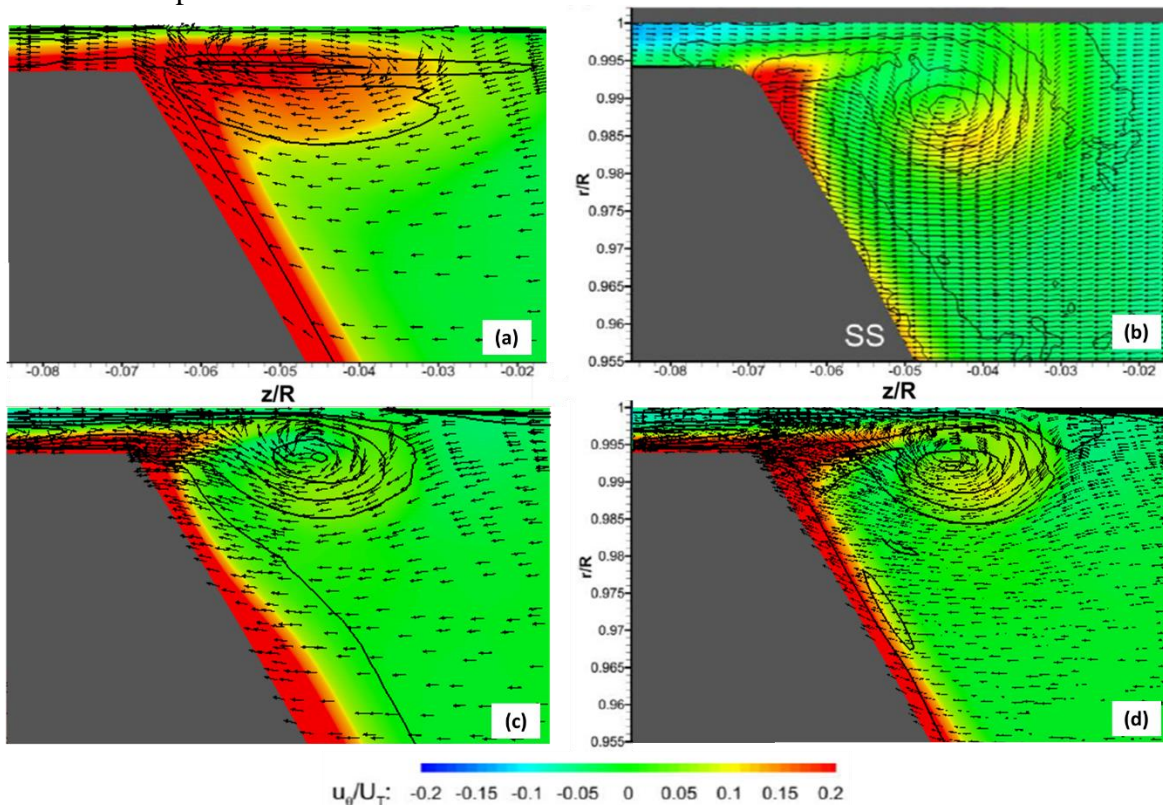


Figure 36. U_θ/U_T distribution, ω_θ isolines and scaled vectors in the plane $s/c = 0.131$ with: a) coarse mesh, b) experimental result [1], c) fine mesh and d) refined tip mesh

4. STEADY RANS SIMULATIONS

Looking at vorticity distributions it becomes easier to analyze the “endwall boundary layer separation region” as defined in Li et. al [1]. This separation region is only present for the finer mesh and still its length is slightly bigger in the experiment (Figure 37).

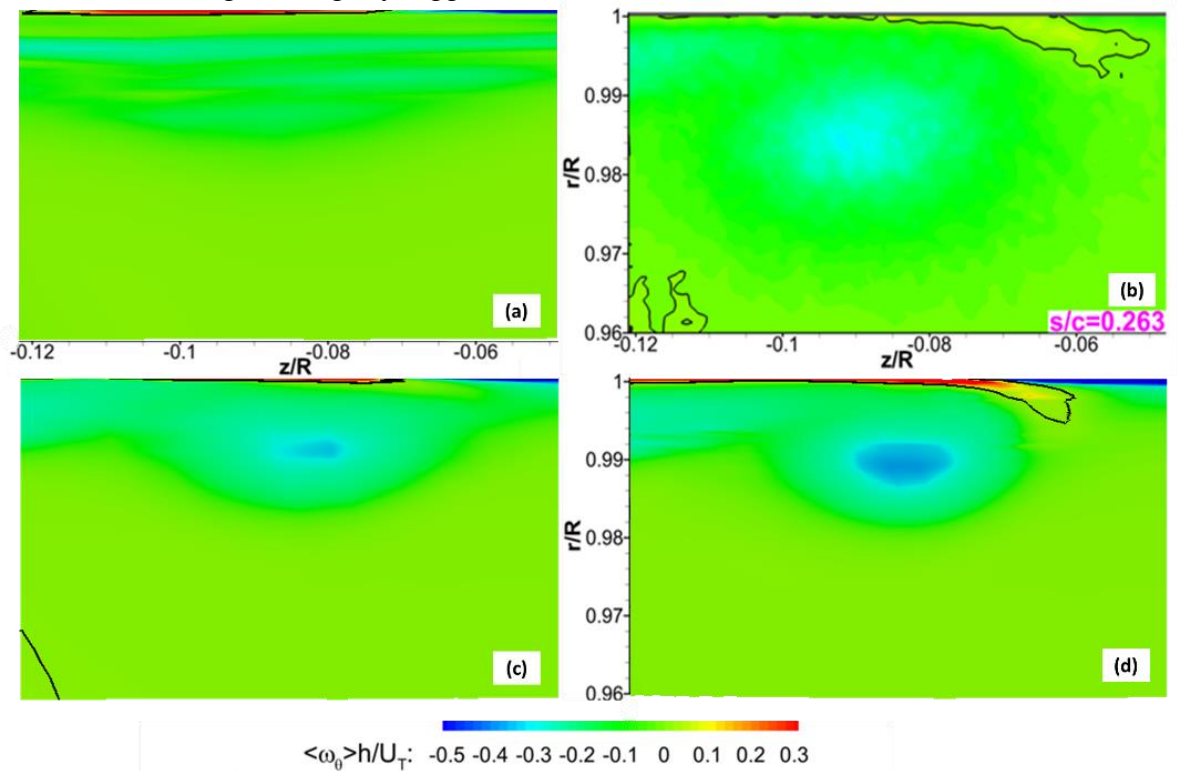


Figure 37. $\omega_\theta h / U_T$ distribution and $\omega_\theta = 0$ isolines in the plane $s/c = 0.263$ with: a) coarse mesh, b) experimental result [1], c) fine mesh and d) refined tip mesh

4.2.5. Divergence scheme

For higher accuracy, it is convenient to use higher order schemes to reduce truncation error. This procedure can be done by different schemes present in the OpenFOAM library. The following schemes will be compared: upwind, linearUpwind and limitedLinear. The upwind scheme is first order accurate, whereas linearUpwind and limitedLinear are considered as second order, providing higher accuracy. This implies better definition of the TLV and less error in performance prediction.

First, performance parameters can be compared between the three schemes as seen in Figure 38. The limitedLinear scheme seems to give worse performance prediction, although it is of only 1%.

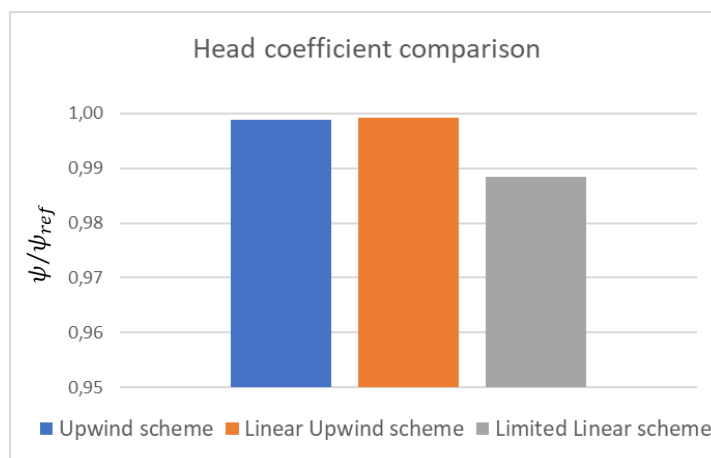


Figure 38. Head coefficient comparison for different divergence schemes.

Additionally, the experimental planes are compared as in Figure 39 and Figure 40. The upwind scheme is not capable of predicting correctly the vortex and it appears attached to the tip. Both second order schemes predict the vortex more separated from the tip of the blade. LimitedLinear shows a stronger vortex structure than linearUpwind, resembling better the experimental results. Looking at the last plane in Figure 40, similar trends can be observed.

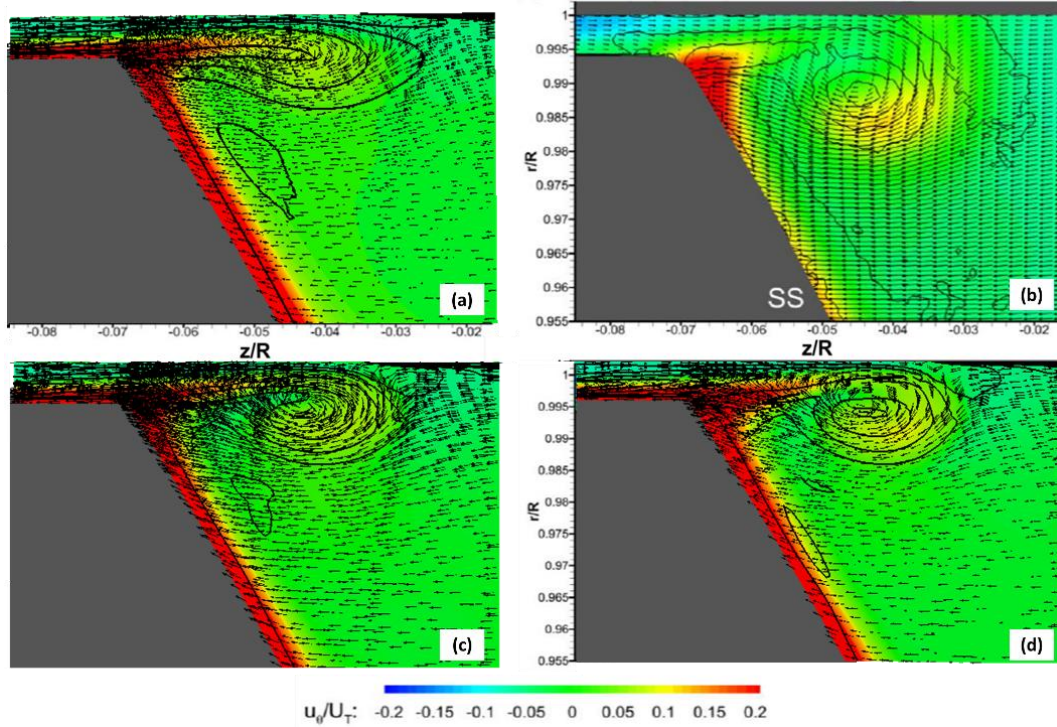


Figure 39. U_θ/U_T distribution, ω_θ isolines and scaled vectors in plane $s/c=0.131$ where: a) upwind scheme, b) experimental result [1], c) linear upwind and d) limited linear.

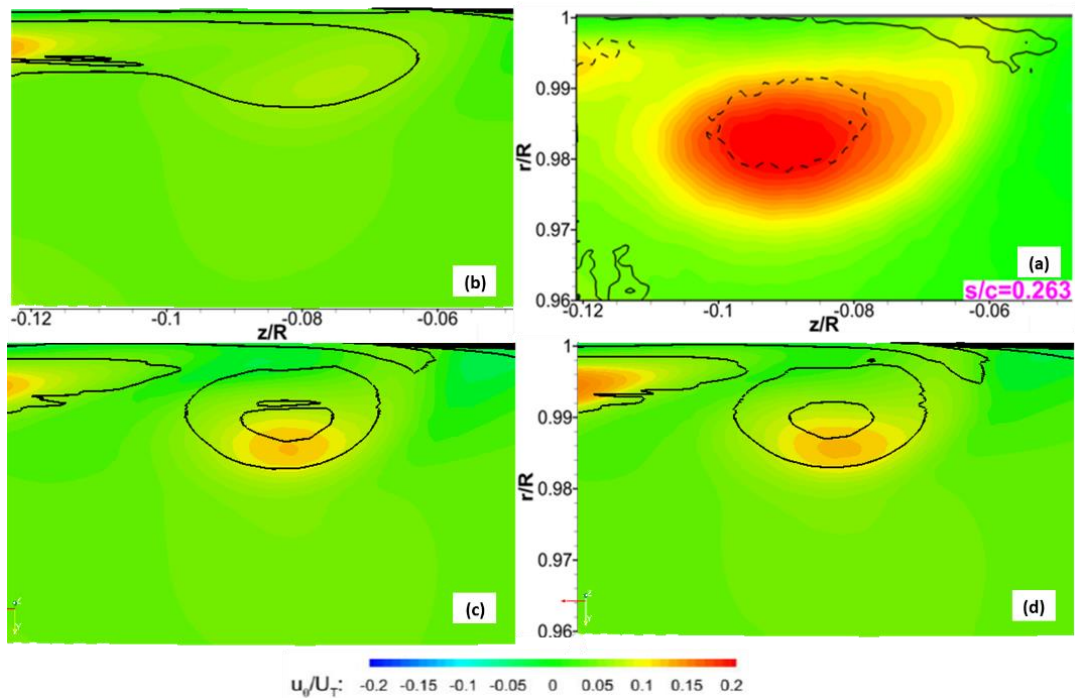


Figure 40. U_θ/U_T distribution and ω_θ isolines in plane $s/c=0.263$ where: a) upwind scheme, b) experimental result [21], c) linear upwind and d) limited linear.

4. STEADY RANS SIMULATIONS

4.3. Wall functions

Wall functions allow for a coarser mesh in the normal-wall direction while providing qualitative good results. Correct application of wall function includes assuring a y^+ value over 30 in the first row of cells close to the wall. Therefore, only the log-law region will be resolved, whereas the buffer and viscous sub-layer will be modeled. The wall functions used for this project are:

1. `kqRWallFunction` for TKE
2. `omegaWallFunction` for ω
3. `nutUSpaldingWallFunction` for turbulent viscosity

Considering the implementation of these wall functions in OpenFOAM, only the TKE wall function is strictly restricted to y^+ over 30. The other wall functions are blended in order to work properly for y^+ values within the viscous sub-layer and log-law region [23].

Two main regions can be seen in Figure 41, where the lower y^+ values correspond to where the mesh was refined, that is, between the blade LE and its mid-chord length. In that region is where the TLV appears and needs to be correctly predicted, so correct boundary layer prediction is crucial. The y^+ value in the refined region stays approximately within the viscous sub-layer so the TKE wall function is not correctly applied in that zone.

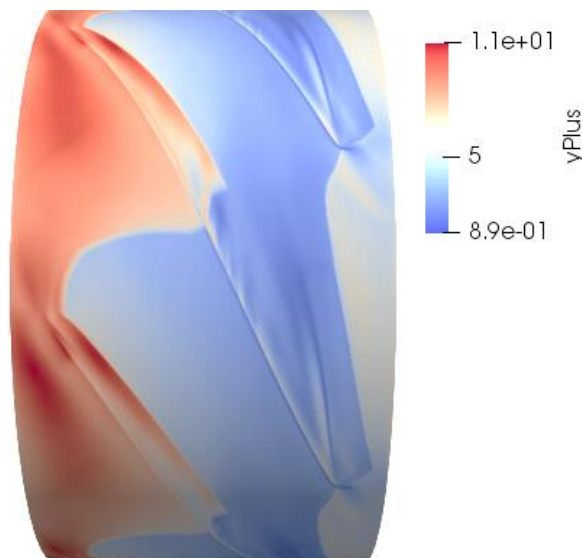


Figure 41. y^+ values for finer mesh in the shroud surface.

From Figure 42, it can be concluded that in the refined region on the blades the y^+ value is approximately between 5 and 20. In this case, all cells are located in the buffer layer and TKE wall function will introduce modeling errors.

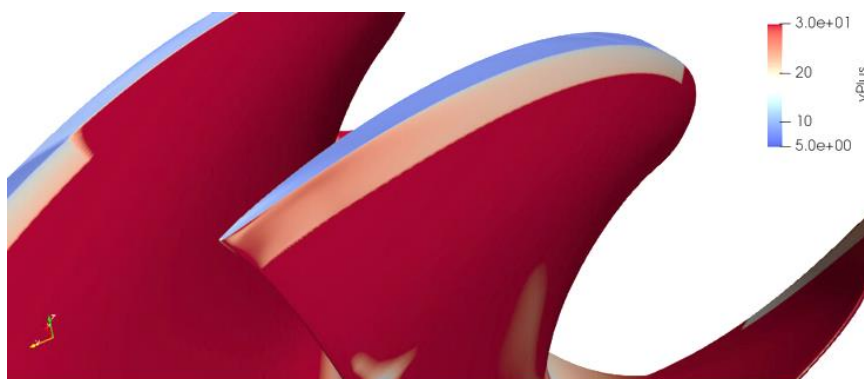


Figure 42. y^+ values for finer mesh in the blade surface.

As the space available for discretizing the tip gap is very limited, the only possible solution would be to resolve the full boundary layer applying a low Reynolds model for the TKE. This is not done during the scope of the project, so this limitation should be considered when analyzing the results.

4.4. Rotor-stator interface

As the approach used for simulating the rotation approach is MRF (frozen rotor), each blade will have a different location in relation to the stator blades. Using sliding mesh in URANS and averaging along a whole cycle, removes this dependency.

Studying the SPIV pictures at each rotor blade can provide an idea of how important this interaction between stator and rotor is for TLV prediction. The last plane studied ($s/c = 0.263$) should be more influenced by the frozen rotor approach as it is closer to the blade trailing edge (TE) and to the stator blades.

Results correspond to the 4D inlet case with uniform velocity profile and $k-\omega$ SST model. However, the conclusions can be extrapolated to any of the cases analyzed during this project. From Figure 43, no remarkable difference can be seen at the first plane, which is further away from the TE of the blade. At the last plane (Figure 44), which is closer to the stator blades, there is still no visible difference between the blades. The interaction between stator and rotor is weakly noticed by the rotor, not modifying abruptly the TLV structures between blades for the frozen rotor approach.

4. STEADY RANS SIMULATIONS

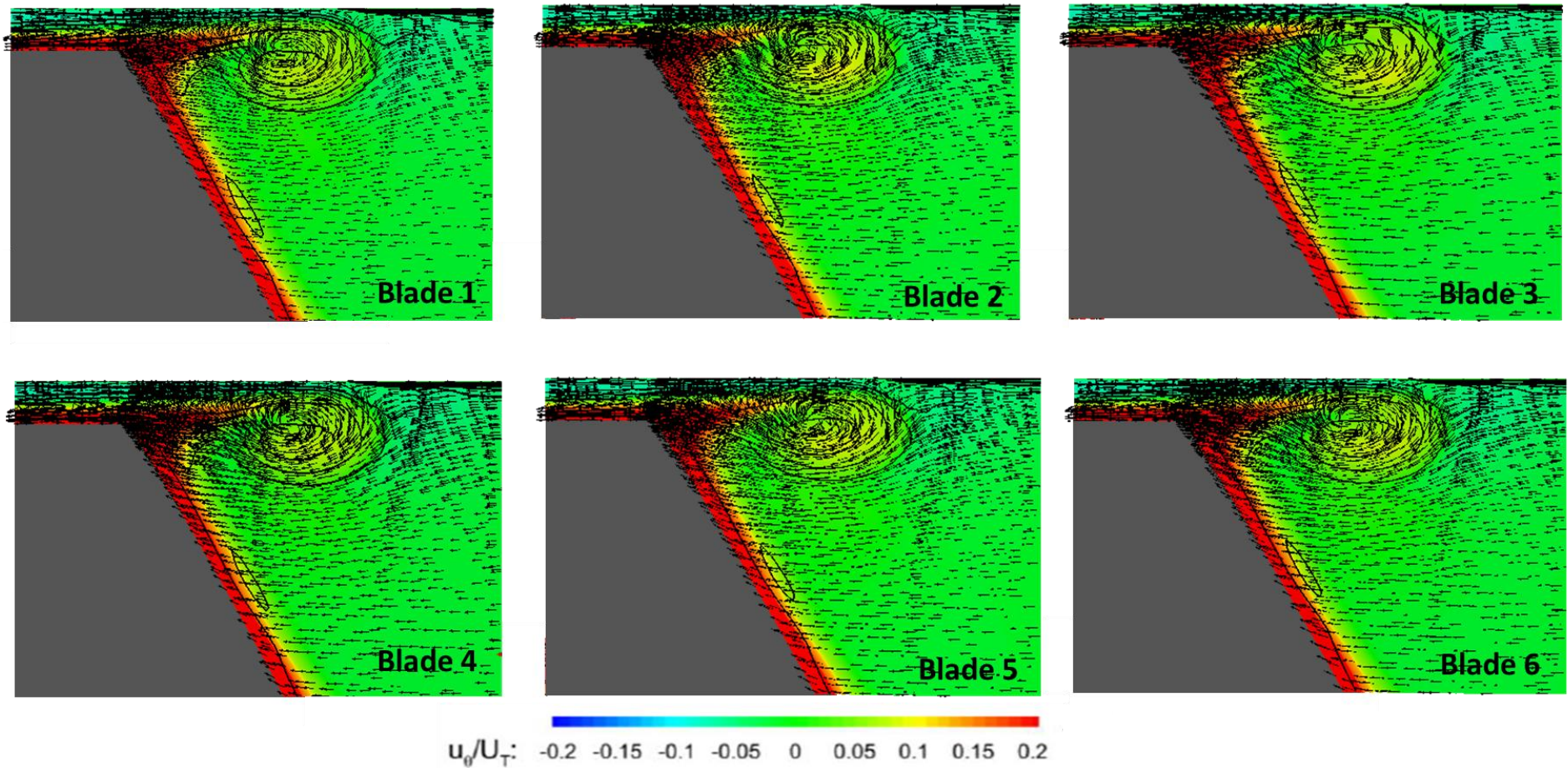


Figure 43. U_θ/U_T distribution, ω_θ isolines and scaled vectors comparison for each rotor blade comparison for MRF at plane $s/c = 0.131$ (along the rotation direction)

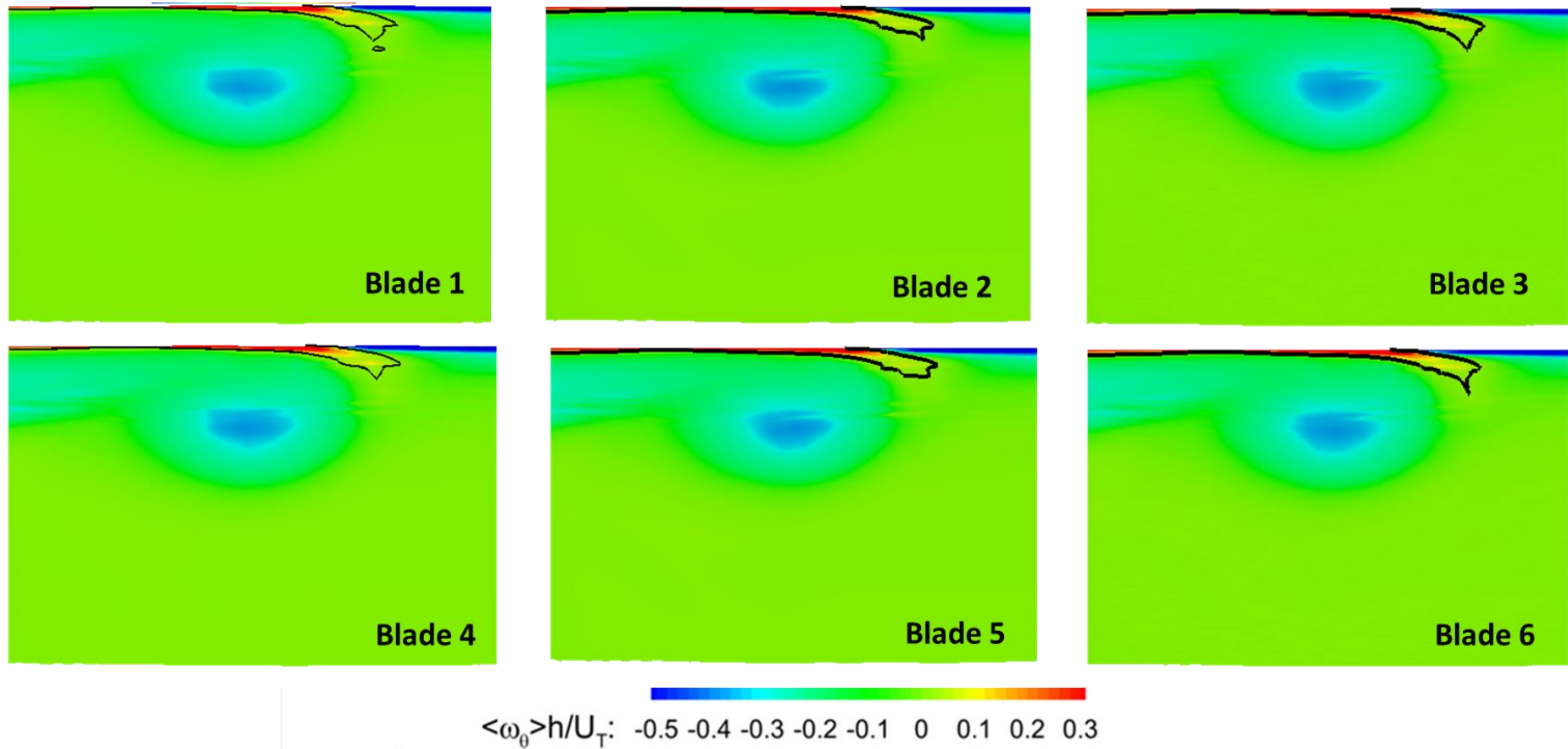


Figure 44. $\omega_\theta h / U_T$ distribution and $\omega_\theta = 0$ isolines comparison for each rotor blade for MRF at plane $s/c = 0.263$ (along the rotation direction).

4. STEADY RANS SIMULATIONS

4.5. Blade geometry

The geometry for the aluminum model of the AxWJ-2 does not have fillets on the pressure and suction edges of the blades as seen in Figure 45 a) and Figure 46 a). However, in Li et al. [1] the model used is acrylic and does have rounded edges but the value of that radius is not reported.

An important difference between simulations and experiment is the existence of a recirculation bubble in the clearance gap (section 4.1.2). It influences the strength of the tip leakage flow coming to the blade SS edge and the formation of the TLV structure and endwall boundary layer. For studying if that recirculation bubble disappears or is reduced for a smoother edge of the blade, the radius from the experimental plane $s/c = 0.131$ is measured and used as a guide for modifying the geometry. This modification is done using the software Pointwise.

From the experimental plane $s/c = 0.131$, two lines are drawn following the top side and SS of the blade (obtaining the shape of the geometry without fillet). The distance between that new vortex and the start of the rounded edge on the top side of the blade is measured, as well as the distance from the vertex to the start of the fillet in the suction side. These distances define the points in the mesh where the rounded edge should start. From that, only a constant is defined in Pointwise to try to resemble the curvature of the edge by guess, comparing with the experimental image. The result can be seen in Figure 45 b).

Two additional cases with increased radius are created to analyze the trend of the analysis, shown in Figure 45 c) and d). All cases are studied for an inlet duct of 4D with uniform inlet velocity profile, $k - \omega SST$ turbulence model and steady MRF simulations.

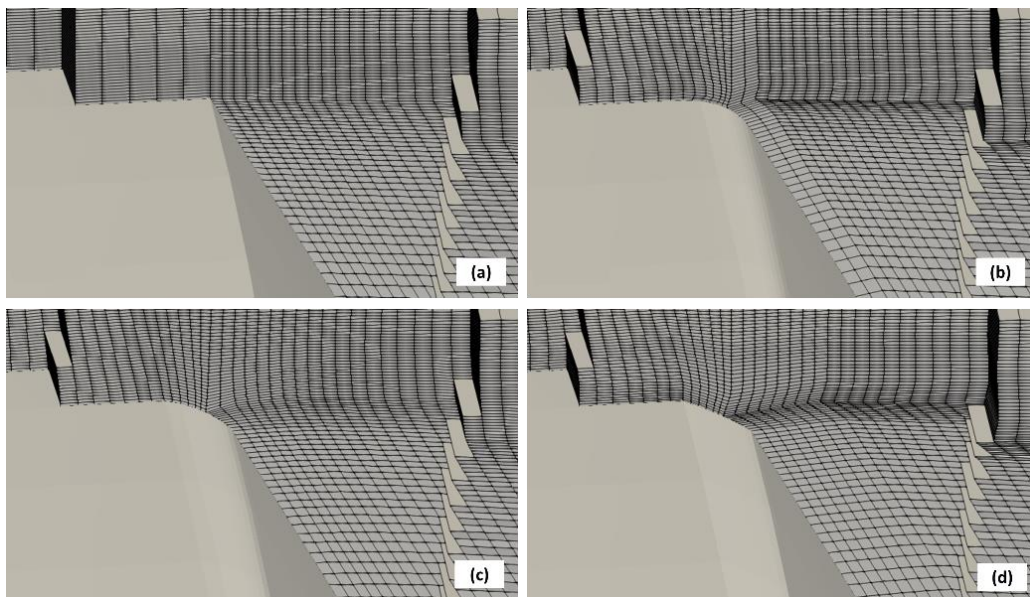


Figure 45. Mesh comparison at the blade edge of the SS for: a) no fillet, b) 1st fillet, c) 2nd fillet and d) 3rd fillet case.

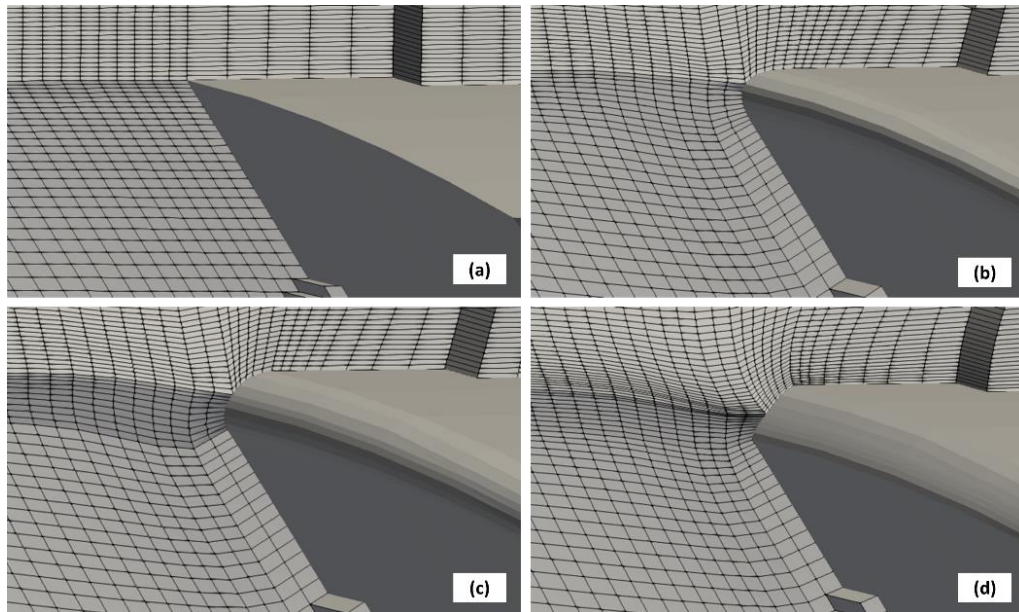


Figure 46. Mesh comparison at the blade edge of the PS side for: a) no fillet, b) 1st fillet, c) 2nd fillet and d) 3rd fillet case.

4.5.1. Performance

From Figure 47, it can be seen a reduction trend in the head coefficient as the radius increases. It must be considered that the reference value of the head coefficient corresponds to the aluminum geometry (without fillet). As the increase in radius generates a higher tip leakage flow and a stronger TLV, the head coefficient may be reduced because of the increase in losses. This trend can be observed in Figure 48, where the pressure difference between the PS and SS of the blade increases as the radius does. For obtaining this chart, the mean pressure values at the PS and SS of the tip gap region were calculated, therefore a negative value of pressure difference means that there is higher flow rate against the leakage flow direction (due to the recirculation bubble).

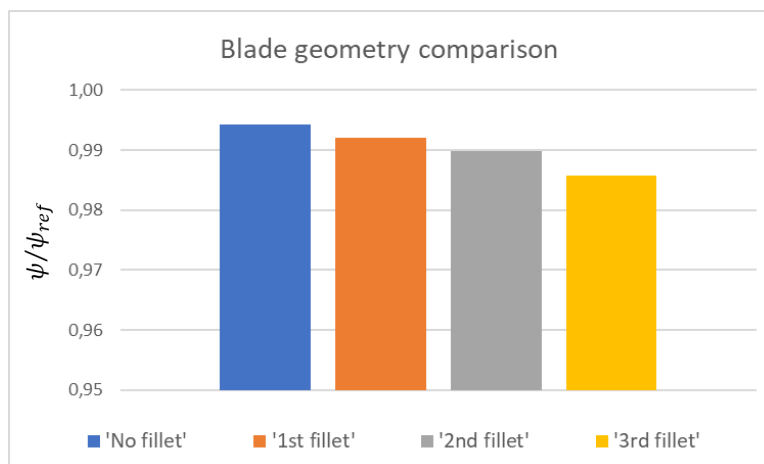


Figure 47. Head coefficient comparison for different blade geometries.

4. STEADY RANS SIMULATIONS

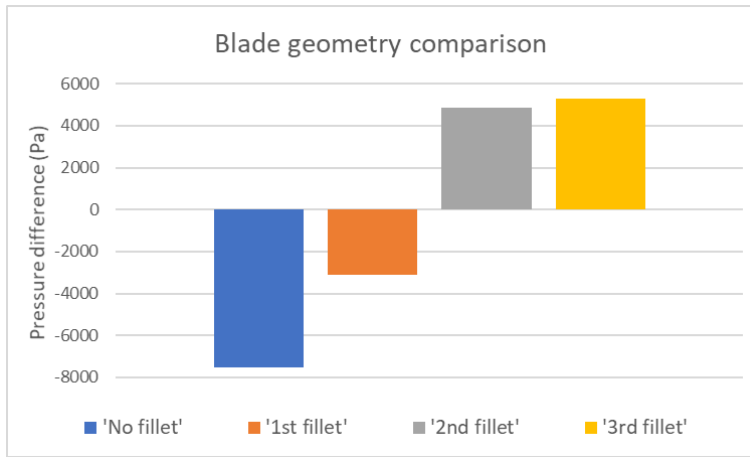


Figure 48. Pressure difference between the PS and SS of the blades for each fillet case.

4.5.2. SPIV planes

From this study, it is expected to see an influence in the strength and location of the TLV as the radius of the blade edge is increased. This phenomenon is observed in Figure 49, where the tangential velocity of the TLV increases with the radius. Also, the vortex is moved away from the blade edge into the core passage. However, in the experiment the TLV is even closer to the core flow passage but its tangential velocity is not that high as in Figure 49 e). Even though the radius value from experiments is unknown, it seems to be between the no fillet and the 1st fillet case by looking at Figure 49.

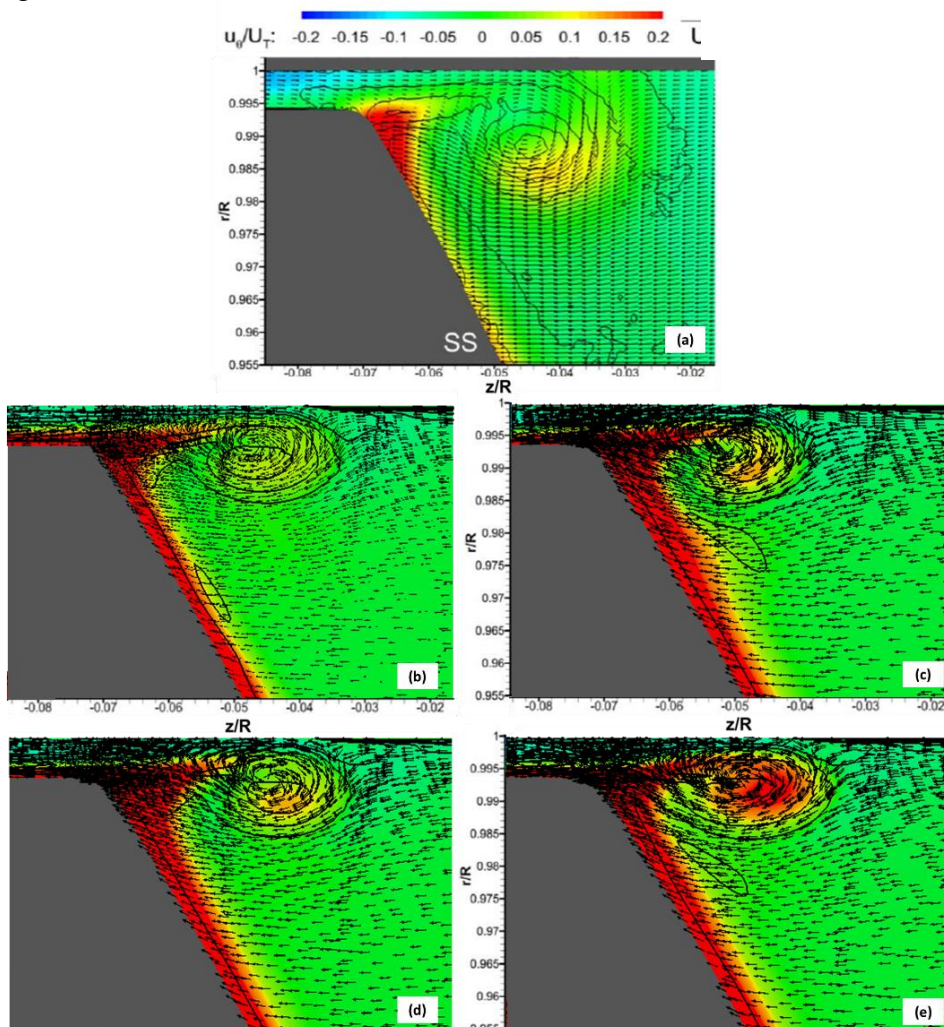


Figure 49. U_θ/U_T distribution, ω_θ isolines and scaled vectors in plane $s/c = 0.131$ where: a) experimental data [1], b) no fillet, c) 1st fillet, d) 2nd fillet and e) 3rd fillet case.

However, the recirculation bubble is still present for all the cases but its size is reduced by smoothing the shape of the edge at the PS of the blade (Figure 50). This change is mainly visible between a), b) and c), not so for the 3rd fillet case. This last fillet has slightly sharper edges than the 1st and 2nd fillet cases.

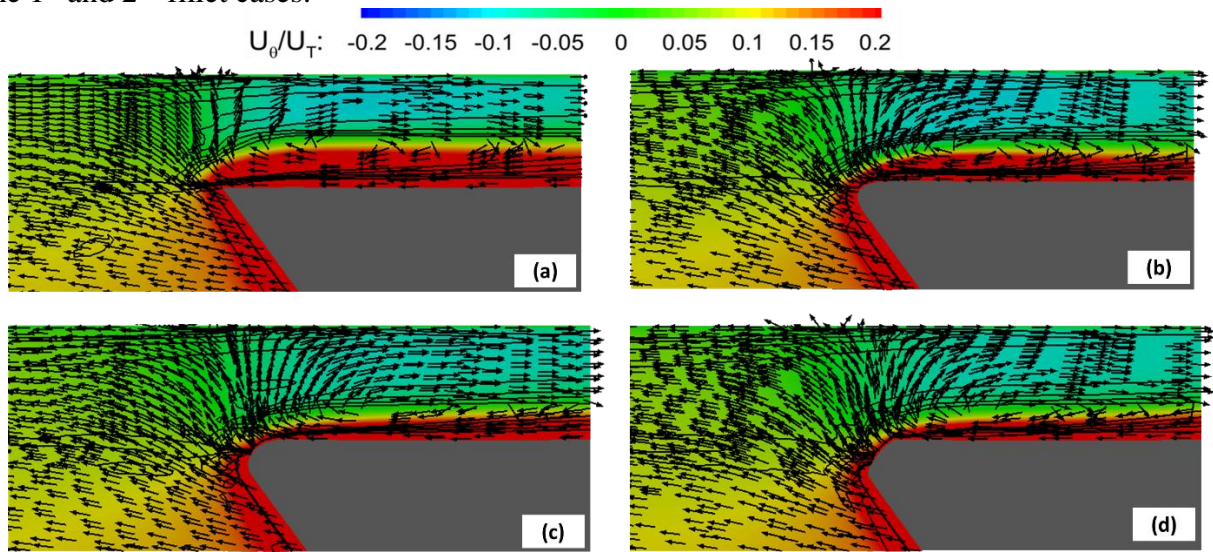


Figure 50. U_θ/U_T distribution, ω_θ isolines and scaled vectors on the PS of the blade for plane $s/c = 0.131$ where: a) no fillet, b) 1st fillet, c) 2nd fillet and d) 3rd fillet case.

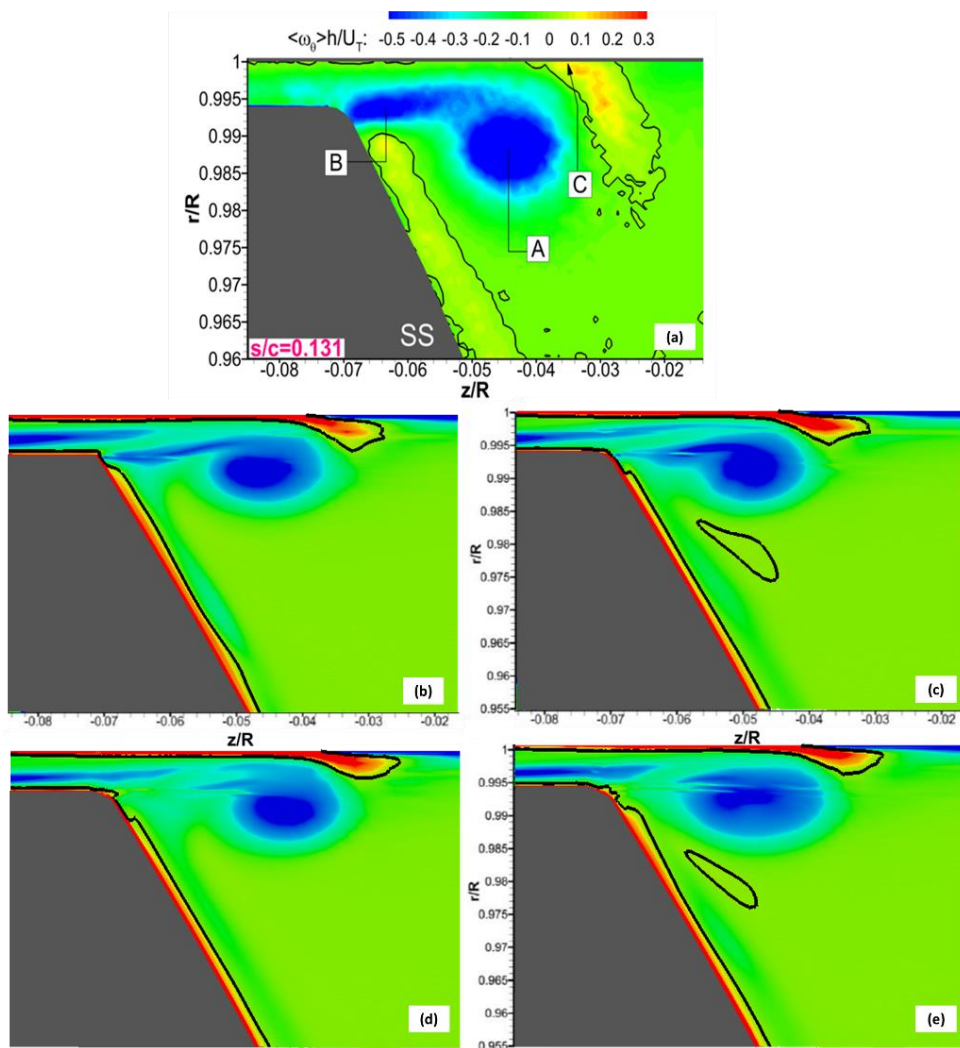


Figure 51. $\omega_\theta h/U_T$ distribution and $\omega_\theta = 0$ isolines in plane $s/c = 0.131$ where: a) experimental data [1], b) no fillet, c) 1st fillet, d) 2nd fillet and e) 3rd fillet case.

4. STEADY RANS SIMULATIONS

Looking at the first plane ($s/c = 0.131$) in terms of tangential vorticity, the TLV tends to detach from the blade, disappearing the shear layer at the edge (Figure 51 e). On the other hand, the endwall boundary layer separation is not affected by the shape of the blade.

4.6. Grid convergence study

A grid convergence study is performed in terms of global quantities, specifically, the total pressure drop. The meshes used for the analysis include the coarse, medium and fine mesh (Figures 5-7). The refined tip mesh will not be used as the refinement only applies to the tip region and not the whole rotor. The procedure used for doing the convergence study is presented in “Procedure for Estimation and Reporting of Uncertainty Due to Discretization in CFD Applications” [24].

The grid refinement factor is calculated as the ratio between the number of cells in the rotor for each mesh (Table 2). This way, $r_{32} = 2.61$ and $r_{21} = 2.43$ where 1 corresponds to the fine mesh, 2 for the medium and 3 to the coarse mesh. The ‘observed’ order of convergence is 2, as the limitedLinear scheme was used. The value obtained for the calculated order of convergence P is 2.36 which is very close to the ‘observed’ value. Figure 52 shows the values for pressure drop for the three meshes studied as well as the extrapolated value (0 normalized grid spacing). The estimated error for the fine mesh solution is 0.3%, according to the Grid Convergence Index (GCI) calculations.

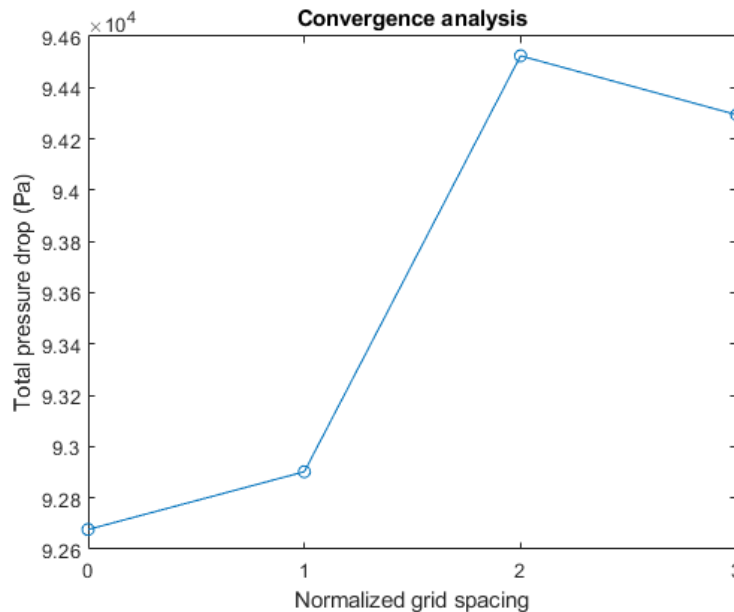


Figure 52. Convergence study for pressure drop.

5. UNSTEADY RANS SIMULATIONS

Hereafter unsteady simulations using a Sliding Mesh (SM) approach will be performed. Some set-up properties are defined from the parametrical studies conducted in the steady MRF simulations.

5.1. Validation of results

5.1.1. Performance prediction

In Figure 53, there is a performance comparison between the SM and MRF simulations, both for a 4D inlet duct with uniform velocity profile and $k - \omega SST$ turbulence model. Although the unsteady results provide a lower head coefficient ratio according to Figure 53, the deviation related to the MRF prediction is of only 0.6%.

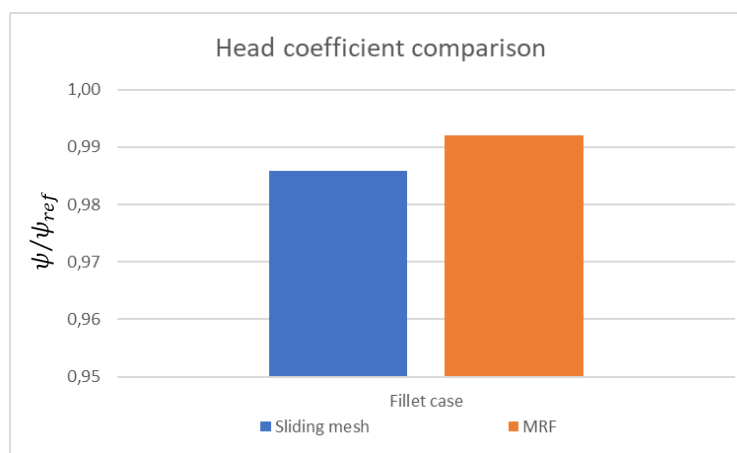


Figure 53. Head coefficient comparison between MRF and SM simulations.

5.1.2. TLV structures

In order to compare the simulation results with the experiment, main variables like velocity, are averaged. The averaging performed in the experiment was done only at the measurement plane for every cycle throughout 1000 cycles [1]. However, averaging over 1000 revolutions is not feasible for a CFD simulation. Considering that all blades in the geometry have the same tip gap (as explained in section 3.2) and stator-rotor interaction is weak (regarding section 4.4), averaging for every cell over a whole cycle would give a good approximation to the experimental method.

In Figures 55-57, the URANS results for the 1st fillet case with 4D inlet, $k - \omega SST$ model and uniform inlet profile are presented. It can be seen a better agreement for the unsteady simulations than for the steady simulations performed in the previous chapter. Still, some discrepancies with the experiment remain, such as the recirculation bubble in the tip gap (as the geometry is the same as in the MRF simulation). However, its effect on the TLV is stronger compared to the MRF results (Figure 57).

5. UNSTEADY RANS SIMULATIONS

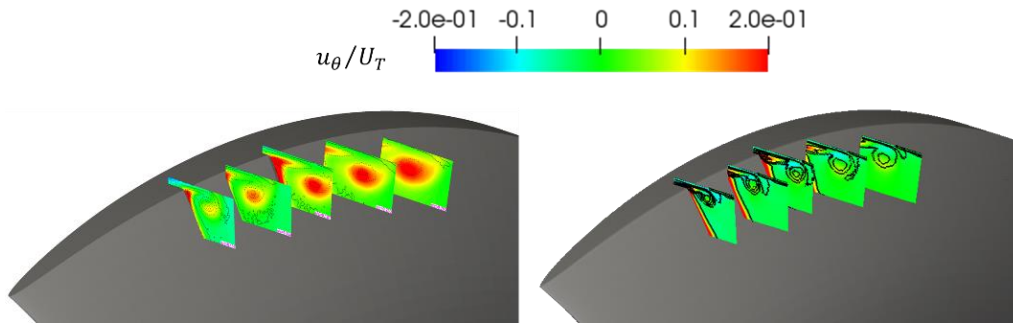


Figure 54. U_θ/U_T distribution and ω_θ isolines for each measurement plane, where the left figure corresponds to the experiment [1] and the right one to the SM 1st fillet case.

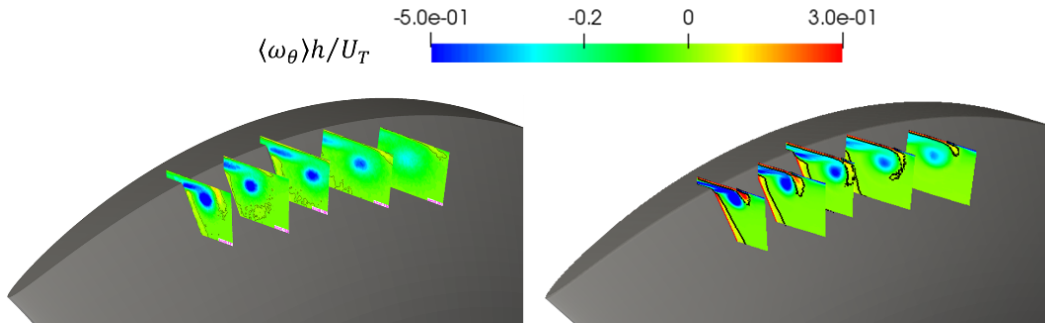


Figure 55. $\langle \omega_\theta \rangle h/U_T$ distribution and $\omega_\theta = 0$ isolines for each measurement plane, where the left figure corresponds to the experiment [1] and the right one to the SM 1st fillet case.

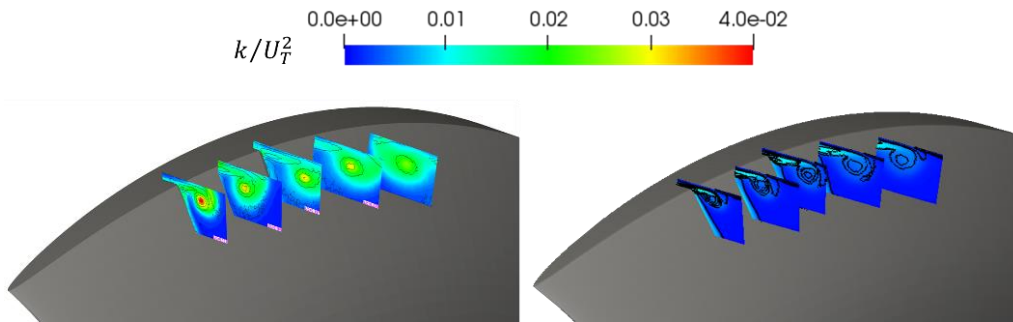


Figure 56. k/U_T^2 distribution and ω_θ isolines for each measurement plane, where the left figure corresponds to the experiment [1] and the right one to the SM 1st fillet case.

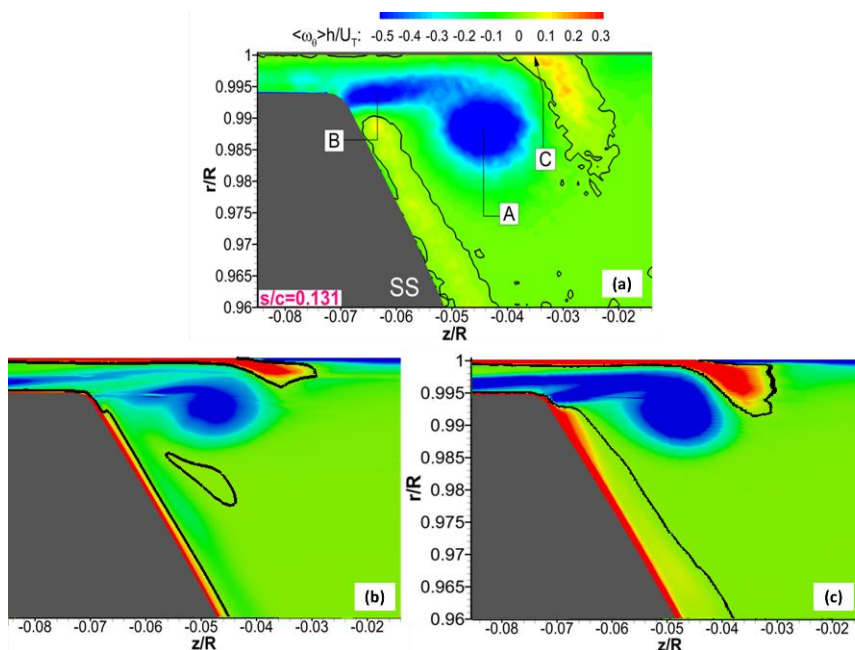


Figure 57. $\langle \omega_\theta \rangle h/U_T$ distribution and $\omega_\theta = 0$ isolines for plane $s/c = 0.131$ with: a) experimental results [1], b) MRF and c) SM simulation.

In the last experimental plane, there is an increase in tangential velocity and reduction in tangential vorticity due to a ‘bursting’ phenomena [1]. In both, MRF and SM simulations, the tangential velocity and vorticity are far from expected in the last plane. Therefore, other planes further downstream in the TLV trajectory are analyzed in order to find this ‘bursting’. Results show that the vortex bursting seen in plane $s/c = 0.263$ in the experiment is encountered further downstream in the simulations (plane $s/c = 0.55$, Figure 58 a). For another plane located at $s/c = 0.585$, the region with high tangential velocity increases in size, occupying a big portion of the analyzed plane (Figure 58 c). It has to be considered that these planes are located in a different x-axis range due to the trajectory of the vortex.

Bursting appears due to instabilities in the vortex when its relative velocity becomes smaller (or high tangential velocity in an absolute frame of reference). These instabilities are damped by the turbulence model, stabilizing the vortex. Furthermore, divergence schemes may also affect the location of the vortex bursting as a more diffusive behavior damps the instabilities that generate bursting.

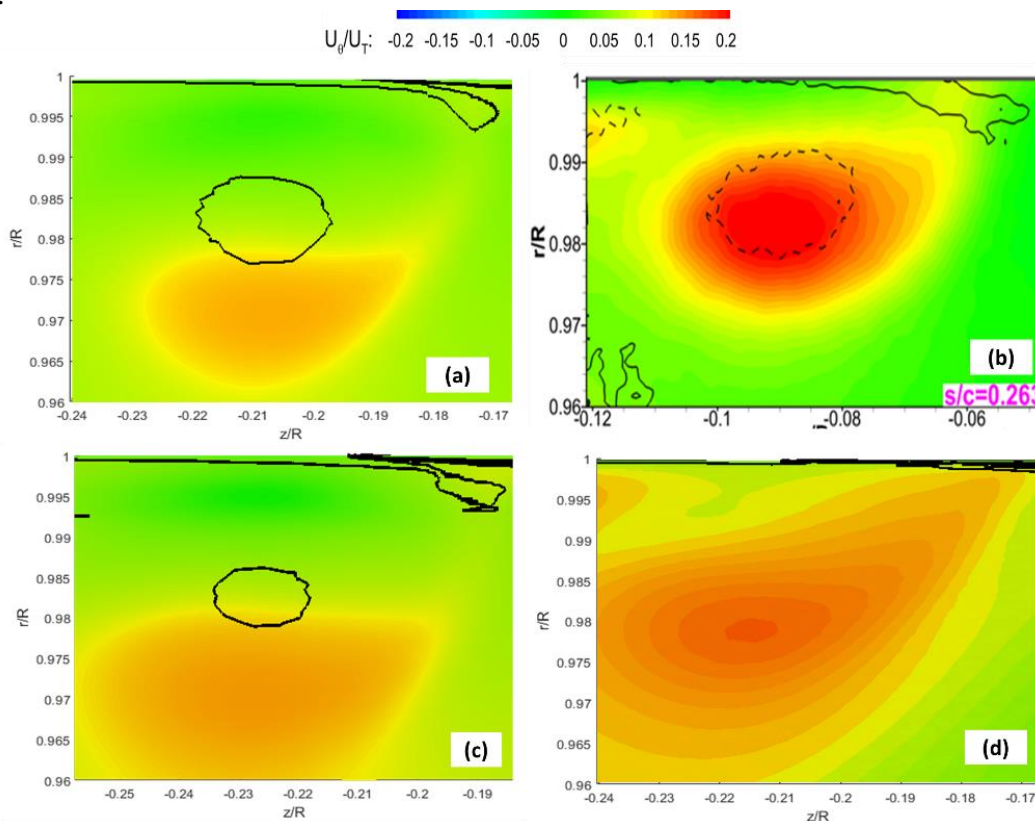


Figure 58. U_{θ}/U_T distribution and ω_{θ} isolines for 1st fillet case with: a) plane $s/c = 0.55$ SM case, b) experimental plane $s/c = 0.263$ [1], c) plane $s/c = 0.585$ SM case and d) plane $s/c = 0.55$ MRF case.

In addition, this bursting planes are compared for MRF and SM simulations. Results show that the bursting plane is further downstream for the unsteady simulation, as the tangential velocity is higher for the MRF case in the plane $s/c = 0.55$ (Figure 58 d). However, MRF simulations can’t resolve an unsteady behavior as turbulence is modelled and time is not resolved in the transport equations. This high tangential velocity region can be produced by the turbulence modeling, but shouldn’t be considered as a prediction of bursting.

Another parameter studied for this simulation is the normal Reynolds stresses. As a turbulence model is used, fluctuations from velocity can’t be used for obtaining the stresses. Most of these fluctuations will be ‘stored’ inside the turbulence parameters k , ω and μ_T . For extracting those stresses from the turbulence model, a hand derivation was performed as explained in ‘Appendix I: Reynolds stresses derivation’. From Figure 59, it can be seen how inaccurate turbulence models can be for Reynolds stresses prediction as turbulence models don’t represent physics. Stresses are isotropic as expected from the turbulence model assumptions [13].

5. UNSTEADY RANS SIMULATIONS

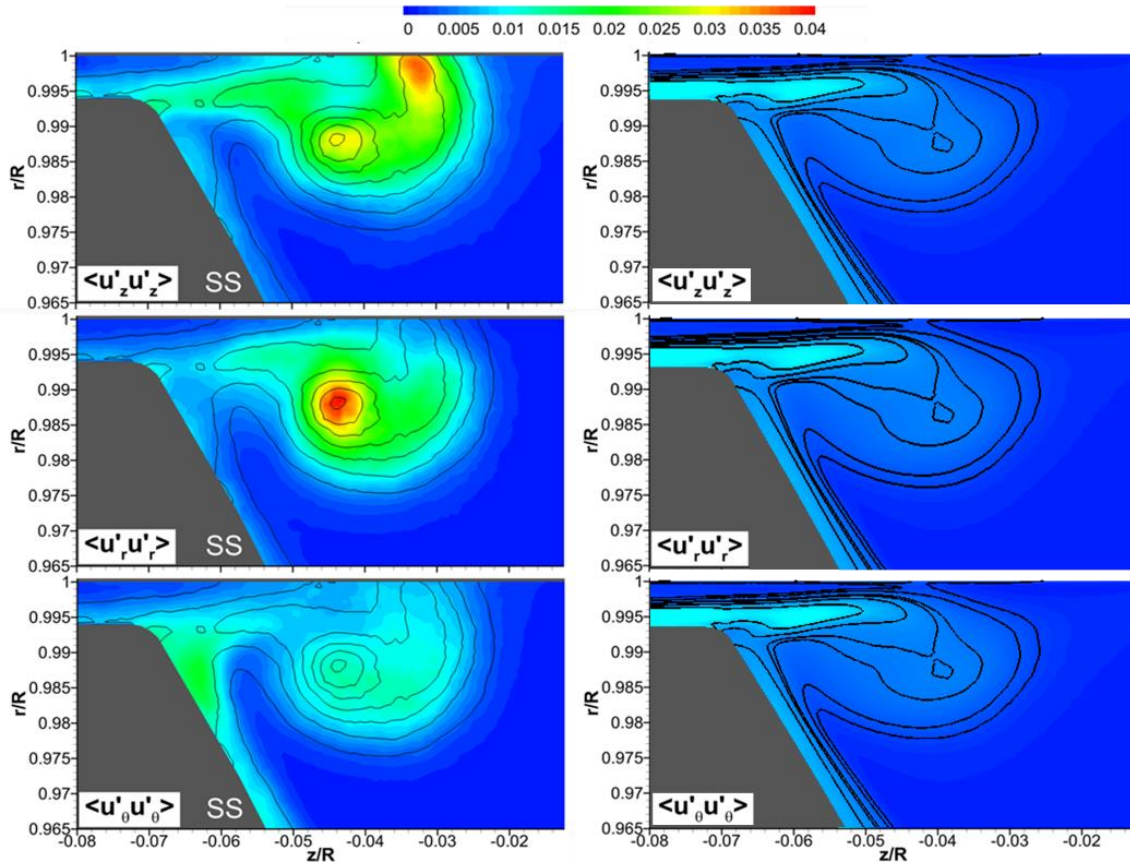


Figure 59. Adimensional normal Reynolds stresses (divided by U_T^2) distributions with TKE isolines for $s/c = 0.131$ for the SM 1st fillet case (right) and experimental data (left).

5.2. Turbulence model comparison

In this case, unlike for the MRF turbulence study, the $k - \omega$ SST SAS model is compared. This model aims to behave like a LES formulation for the unsteady flow regions and like a URANS model for the steady regions. This model is then able to adapt the equations by means of the von Karman length scale, which is introduced in the transport equations [25].

5.2.1. Performance prediction

From Figure 60, it can be concluded that both models predict similar head coefficients.

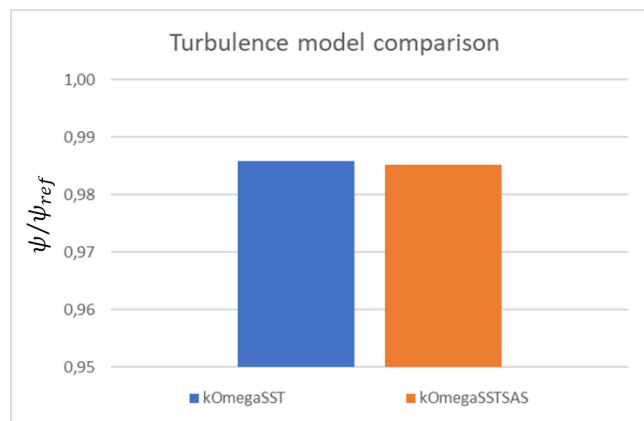


Figure 60. Head coefficient prediction comparison for the $k - \omega$ SST and $k - \omega$ SST SAS model.

5.2.2. TLV structures

When comparing the TLV prediction between both models, there is no remarkable difference in the first plane as observed in Figure 61. However, differences accentuate for the last plane (Figure 62), but SAS model doesn't resemble better the experimental data.

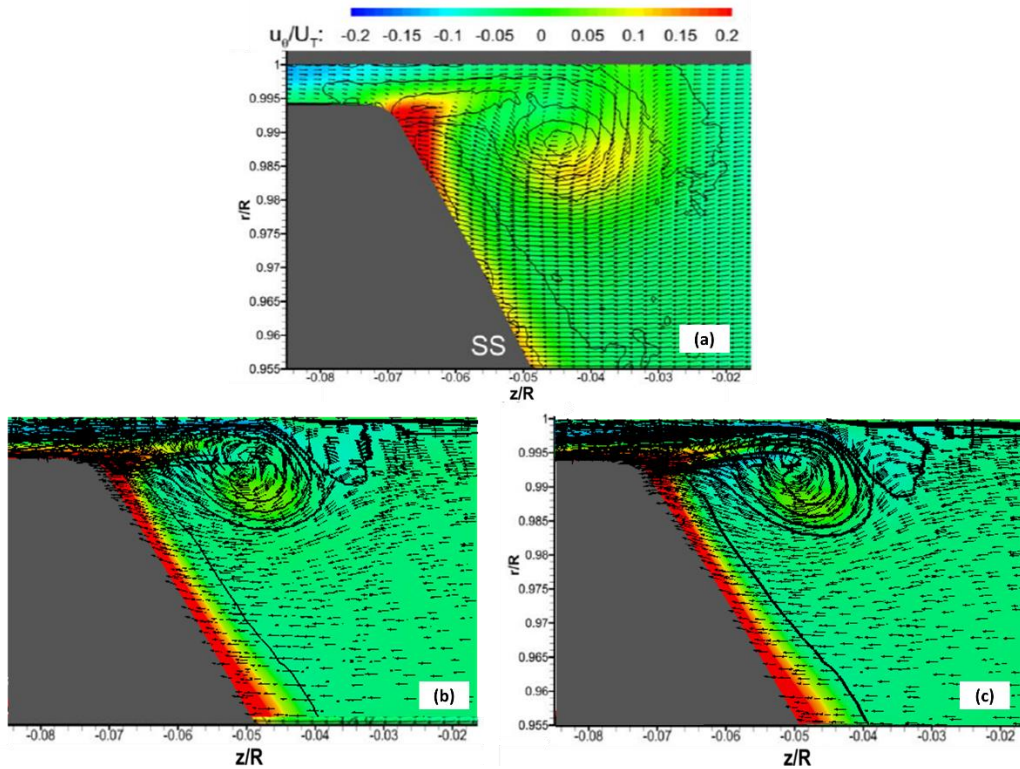


Figure 61. U_θ/U_T distribution, ω_θ isolines and scaled vectors in plane $s/c = 0.131$ where: a) experimental data [1], b) $k - \omega$ SST and c) $k - \omega$ SST SAS model.

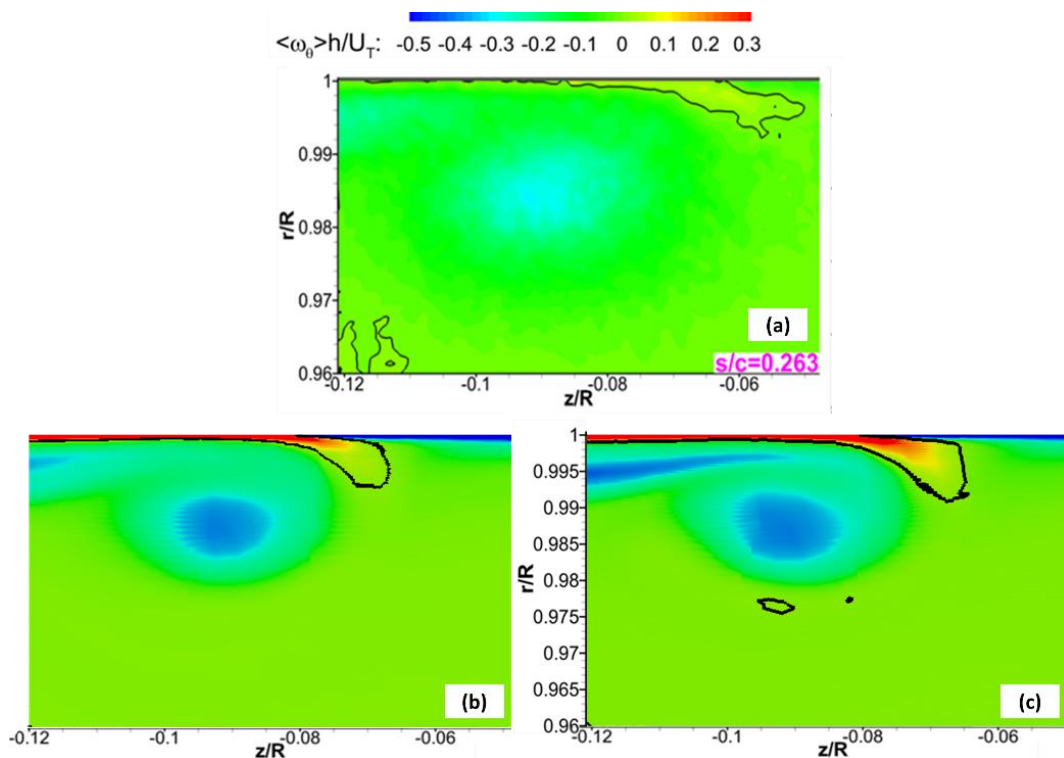


Figure 62. $\langle \omega_\theta \rangle h/U_T$ distribution and $\omega_\theta = 0$ isolines in plane $s/c = 0.263$ where: a) experimental data [1], b) $k - \omega$ SST and c) $k - \omega$ SST SAS model.

5. UNSTEADY RANS SIMULATIONS

A possible cause why the SAS model does not provide better agreement in TLV prediction is the Courant-Friedrichs-Levy (CFL) number used for the simulations. The value was set to 36 which is too high for resolving turbulence in the TLV (usually around 1). However, such reduction in the CFL is not feasible for this simulation. Also, before the LES formulation becomes active because of unsteadiness, RANS formulation has damped the instabilities within the vortex. That stabilizes the vortex along its trajectory retarding the appearance of vortex breakdown.

6. CONCLUSIONS

Studies conducted in this thesis provide qualitatively good agreement with experimental data [1] and define a procedure for adequately predicting TLV structures. All simulations are performed using RANS models for steady and unsteady mode. However, LES or hybrid RANS/LES simulations should be performed in the future as they can provide more detail in the TLV structure compared to RANS models.

One limitation of the project refers to the use of wall functions. Wall functions for omega and nut have been used adequately, not so for k. A possible continuation of this work could be the analysis of the influence of wall functions (with adequate y^+ for the k wall function) in opposition to resolving up to the wall, or with fully resolved boundary layer where $y^+ < 1$.

Concerning mesh refinement, three meshes with increasing level of refinement have been used for assuring global convergence. For local convergence in the gap region, a fourth mesh was created with refinement only in the tip gap region. A minimum of 40 cells are sufficient in the radial direction covering the tip gap to assure adequate prediction of the TLV structure. This last mesh is used for further parametrical studies conducted in both steady and unsteady conditions.

Most of the parametrical studies were performed under steady-state conditions, which can provide accurate results in shorter time. The rotation approach used for the steady simulations is Multiple Reference Frame (MRF) in which the rotor is frozen. From these studies, the optimum set-up is defined in order to improve agreement with experiments. Conclusions from these parametrical studies include:

A) Turbulence model

Consists of a comparison between $k - \omega SST$ and $k - \omega SST$ with curvature correction model that revealed better agreement for the $k - \omega SST$ model.

B) Boundary layer thickness

For obtaining significantly increasing thicknesses, the length of the inlet duct to the pump is increased generating four different cases. TLV structures observed in these cases show no qualitative change in the SPIV planes nor in the trajectory shown by the Q-criterion. Analysis done to the velocity profiles upstream of the blade LE and flow rate coming from inlet and in the tip gap show similar behavior for all cases, explaining the similitude in TLV prediction.

C) Inlet velocity profile

The velocity profile from experiment at a measurement plane of $z/R = 0.65$ was provided. A polynomial curve was fit into the profile and imposed at the inlet of the fluid domain to resemble experiment conditions. Geometry in the surroundings of the measurement plane modifies the velocity profile set at the inlet patch, differing from the experimental profile. The proposed methods are therefore, not suitable for this purpose. A possible solution would be to obtain the velocity profile data at a measurement plane far from the shaft diameter's expansion. Unfortunately, this information is not available.

D) Divergence scheme

Three different divergence schemes are tested for the same set-up: one of first order and two of second order. It is necessary to use second order scheme to adequately predict TLV structures and the best scheme is proved to be the limitedLinear scheme although it

CONCLUSIONS

predicts a lower head coefficient compared to available data.

E) Blade edge shape

The available geometry corresponds to the aluminum model which has sharp edges on the blade tip. On the other hand, the geometry used in the experiment has rounded edges although the radius value is not known. Therefore, an initial radius is approximated using the experimental plane $s/c = 0.131$ as a guide to modify the initial geometry. Two additional cases with increasing radius are designed.

The blade edge shape has a high impact in the TLV structure. The more rounded the edge is, the stronger the TLV becomes and its core moves into the core flow passage. This is a consequence of the increase in the tip leakage flow coming from the pressure side of the blade. This is associated to a reduction in the recirculation bubble on the PS of the blade. The recirculation region doesn't fully disappear in any of the presented cases, as the shape in the PS of the blade is still too abrupt.

Finally, the optimum set-up consists of the 1st fillet case geometry, a 4D inlet duct's length with uniform inlet velocity profile, $k - \omega SST$ model and limitedLinear scheme for divergence. This set-up is used for unsteady simulations in which rotation is defined by a Sliding Mesh (SM) approach. In this approach, the rotor mesh rotates every time step. Results demonstrated higher accuracy in TLV prediction for the unsteady case.

Additionally, another turbulence model comparison was conducted under unsteady mode using the $k - \omega SST SAS$ model, which resolves the turbulence where flow behaves unsteady. Nevertheless, this model seems to be more sensitive to Courant number which is too high for LES formulation. However, reducing its value is not feasible for this type of simulations. This implies that the best results are obtained using the $k - \omega SST$ model for unsteady mode.

REFERENCES

-
- [1] Y. Li, D. Tan, H. Chen, and J. Katz, “Stereoscopic PIV Measurement of the Flow in the Tip Region of an Axial Waterjet Pump,” presented at the International Symposium on Transport Phenomena and Dynamics of Rotating Machinery, Honolulu, Hawaii, 2016, p. 9.
- [2] D. Y. Tan, R. L. Miorini, J. Keller, and J. Katz, “Flow Visualization Using Cavitation Within Blade Passage of an Axial Waterjet Pump Rotor,” in *Volume 1: Symposia, Parts A and B*, Rio Grande, Puerto Rico, USA, 2012, p. 395.
- [3] M. Brambilla and A. Martino, “Research for TRAN Committee - The EU Maritime Transport System: Focus on Ferries,” p. 108, 2016.
- [4] Bill Thomson, “Still going strong.” Rolls Royce Inc., 2019.
- [5] A. Bonnevie Wollebaek and C. Taylor, “Go with the flow.” Rolls Royce Inc., 2019.
- [6] D. Zhang, L. Shi, W. Shi, R. Zhao, H. Wang, and B. P. M. (Bart) van Esch, “Numerical analysis of unsteady tip leakage vortex cavitation cloud and unstable suction-side-perpendicular cavitating vortices in an axial flow pump,” *Int. J. Multiph. Flow*, vol. 77, pp. 244–259, Dec. 2015.
- [7] H. Gao, W. Lin, and Z. Du, “Numerical flow and performance analysis of a water-jet axial flow pump,” *Ocean Eng.*, vol. 35, no. 16, pp. 1604–1614, Nov. 2008.
- [8] N. W. H. Bulten, *Numerical analysis of a waterjet propulsion system*. Technische Universiteit Eindhoven, 2006.
- [9] “Pump-jet,” *Wikipedia, the free encyclopedia*. 2013.
- [10] D. Tan, Y. Li, I. Wilkes, E. Vagnoni, R. L. Miorini, and J. Katz, “Experimental Investigation of the Role of Large Scale Cavitating Vortical Structures in Performance Breakdown of an Axial Waterjet Pump,” *J. Fluids Eng.*, vol. 137, no. 11, p. 111301, Nov. 2015.
- [11] H. Martinsson and J. Varosy, “CFD simulation of the Wakejet flow,” Chalmers University of Technology, Gothenburg, 2017.
- [12] G. Pan and L. Lu, “Numerical Investigation of a Pumpjet Propulsor Based on CFD,” *Int. J. Control Autom.*, vol. 8, no. 11, pp. 225–234, Nov. 2015.
- [13] H. K. Versteeg and W. Malalasekera, *An introduction to computational fluid dynamics: the finite volume method*, 2nd ed. Harlow, England ; New York: Pearson Education Ltd, 2007.
- [14] O. Petit, “Towards Full Predictions of the Unsteady Incompressible Flow in Rotating Machines, Using OpenFOAM,” Chalmers University of Technology, Gothenburg, 2012.
- [15] I. Sadreghighi, “Essentials of Turbo machinery in CFD,” p. 165.
- [16] “9.3.1. The Multiple Reference Frame Model.” [Online]. Available: https://www.sharcnet.ca/Software/Ansys/16.2.3/en-us/help/flu_ug/flu_ug_sec_mrf.html. [Accessed: 19-Feb-2019].
- [17] “See the MRF development,” *OpenFOAMWiki*, 13-Jun-2009. [Online]. Available: http://openfoamwiki.net/index.php/See_the_MRF_development.
- [18] F. R. Menter, “Two-equation eddy-viscosity turbulence models for engineering applications,” *AIAA J.*, vol. 32, no. 8, pp. 1598–1605, 1994.
- [19] “OpenFOAM: User guide v1812,” *OpenFOAM: User Guide*, 2019-2017. [Online]. Available: <https://www.openfoam.com/documentation/guides/latest/doc/guide-bcs-inlet-turbulent-k-turbulent-intensity-kinetic-energy.html>. [Accessed: 21-Feb-2019].
- [20] “2.2.2.6. The Shear Stress Transport (SST) Model,” 2.2.2. *Two Equation Turbulence Models*. [Online]. Available: https://www.sharcnet.ca/Software/Ansys/16.2.3/en-us/help/cfx_thry/i1302321.html#i1302649. [Accessed: 19-Feb-2019].
- [21] “High Magnification SPIV measurements,” *Laboratory for Experimental Fluid Dynamics*. [Online]. Available:

REFERENCES

- http://web.jhu.edu/fluid_dynamics/Current_Projects/Turbomachinery/Waterjet%20Pump%20II/Results.html.
- [22] “4.15. Curvature Correction for the Spalart-Allmaras and Two-Equation Models,” 4.15. *Curvature Correction for the Spalart-Allmaras and Two-Equation Models*. [Online]. Available: https://www.sharcnet.ca/Software/Ansys/16.2.3/en-us/help/flu_th/flu_th_sec_curv_corr.html. [Accessed: 24-Apr-2019].
- [23] L. Fangqing, “A Thorough Description of How Wall Functions Are Implemented In OpenFOAM,” Edited by Nilsson, H., http://www.tfd.chalmers.se/~hani/kurser/OS_CFD_2016 2016.
- [24] “Procedure for Estimation and Reporting of Uncertainty Due to Discretization in CFD Applications,” *J. Fluids Eng.*, vol. 130, no. 7, p. 078001, 2008.
- [25] “2.7. Scale-Adaptive Simulation Theory.” [Online]. Available: https://www.sharcnet.ca/Software/Ansys/16.2.3/en-us/help/cfx_thry/thry_turb_sas.html.

APPENDIX I: REYNOLDS STRESSES DERIVATION

The simulations performed in this project are based on the $k - \omega$ SST RANS model, where turbulence is modeled by means of three parameters: turbulent kinetic energy k , specific dissipation rate ω and turbulent viscosity μ_T . That way, Reynolds stresses are assumed to be isotropic and behave in a similar way viscous stresses do in Newton's law. Therefore, if k and μ_T are known in every point in space as well as the velocity components, the Reynolds stresses can be obtained from Boussinesq hypothesis:[13]

$$\tau_{ij} = -\rho \overline{u'_i u'_j} = \mu_T \left(\frac{\partial U_i}{\partial x_j} + \frac{\partial U_j}{\partial x_i} \right) - \frac{2}{3} \rho k \delta_{ij}$$

where τ_{ij} represents the Reynolds stresses and δ_{ij} is Kronecker delta.

It must be considered that the aim is to obtain the averaged value of the stresses, and the parameters obtained from averaging over time in OpenFOAM are the cylindrical components of velocity. However, if the gradients of the cylindrical velocity are calculated in OpenFOAM post-processing, the derivative will be performed in cartesian coordinates and not cylindrical. As a consequence, the gradient of the cylindrical velocity will be:

$$\nabla \cdot \mathbf{U}_{cylMean} = \begin{pmatrix} \frac{\partial U_r}{\partial x} & \frac{\partial U_\theta}{\partial x} & \frac{\partial U_z}{\partial x} \\ \frac{\partial U_r}{\partial y} & \frac{\partial U_\theta}{\partial y} & \frac{\partial U_z}{\partial y} \\ \frac{\partial U_r}{\partial z} & \frac{\partial U_\theta}{\partial z} & \frac{\partial U_z}{\partial z} \end{pmatrix}$$

Where $\mathbf{U}_{cylMean}$ represents the averaged value of the cylindrical velocity over one cycle. If the gradient is calculated in the steady simulations, instead of $\mathbf{U}_{cylMean}$, \mathbf{U}_{cyl} will be used.

For calculating the normal stresses as presented in the experimental data:

$$-\rho \overline{u'_\theta u'_\theta} = \mu_T \left(\frac{\partial U_\theta}{\partial \theta} + \frac{\partial U_\theta}{\partial \theta} \right) - \frac{2}{3} \rho k$$

As presented before, the data available from post-processing is the derivatives in cartesian coordinates. The following transformation is proposed:

$$\frac{\partial U_\theta}{\partial \theta} = \frac{\partial U_\theta}{\partial y} \frac{\partial y}{\partial \theta} = \{where y = r \cos \theta\} = \frac{\partial U_\theta}{\partial y} (-r \sin \theta)$$

Inserting this transformation into the previous definition and rearranging:

$$\overline{u'_\theta u'_\theta} = 2 \left(\frac{k}{3} + r \sin \theta \frac{\mu_T}{\rho} \frac{\partial U_\theta}{\partial y} \right)$$

This same procedure can be performed for the rest of the stresses.